NUMERICAL ANALYSIS OF DRYING CRACKS DEVELOPED UNDER FIELD CONDITIONS

A Thesis

by

YICHI DU

Submitted to the Office of Graduate and Professional Studies of
Texas A&M University
in partial fulfillment of the requirements for the degree of

MASTER OF SCIENCE

Chair of Committee,	Marcelo Sanchez
Committee Members,	Charles P. Aubeny
	Haly Neely
Head of Department,	Robin Autenrieth

December 2018

Major Subject: Civil Engineering

ABSTRACT

Naturally occurring soils exhibit swelling and shrinking behavior induced by moisture changes. For example, soils tend to swell upon wetting and shrink during drying. This behavior leads to stresses changes that may exceed the soil strength leading to crack formation, which may in turn close during infiltration phases when the soil becomes wetter and expands. Several geotechnical engineering problems, such as foundations and embankments, are strongly affected by the presence of cracks. The study of crack formation and propagation in porous media is a very complex problem and possesses several challenges. Fracture propagation in this research will be modeled using the mesh fragmentation technique (MFT), which consists in introducing finite elements (FE) with high aspect ratio in between the standard (bulk) elements of the FE mesh. In this dissertation, the Saint-Alban clay excavation-drying case is studied in details and used to validate the MFT. The test site is located in Saint-Alban, 80 km west of Québec City in the Saint Lawrence Valley. Numerical simulations were performed in order to achieve a better understanding of the phenomena behind the formation and propagation of desiccation cracks in soils under natural conditions.

CONTRIBUTORS AND FUNDING SOURCES

Contributors

This work was supervised by a thesis committee consisting of Professor Sanchez and Aubeny of the Department of Civil Engineering and Professor Neely of the Department of Soil and Crop Sciences.

The theoretical formulations for Chapter 3 was discussed with Dr. Sanchez and based on previous work. The theory depicted in Chapter 4 were conducted with aid of my friend Michael Maedo who is a PhD student of civil engineering in Texas A&M University.

All other work conducted for the thesis was completed by the student independently.

Funding Sources

No funding supports this graduate study.

TABLE OF CONTENTS

LIST OF FIGURES

LIST OF TABLES

1. INTRODUCTION

1.1 Motivation

The numerical modeling of desiccation cracks has been drawing more attention in past years. Several geotechnical engineering problems, such as foundations and embankments are strongly affected by the presence of cracks. Meanwhile, the mechanical, hydraulic and thermal properties of the geo-material are also tremendously influenced by the desiccation cracks. It is important to carry out more research on the mechanism behind this influence.

Desiccation cracking in soils has a wide spectrum of environmental, agricultural, and hydrological impacts. The movement of moisture and solutes into and within the soil increases due to the presence of cracks that act as preferential pathways for rapid water movement to deeper layers (Greve, Andersen and Acworth, 2010; Kosmas et al., 1991; Harris et al., 1994). This rapid movement reduces the effectiveness of irrigation and causes fast seepage of nutrients and pesticides away from the plants into deeper layers. This may reduce residence time of contaminates in the unsaturated zone where they are usually absorbed by the plants and degraded by bacteria. It may increase the probability of ground water and/or surface water contamination as well, depending on the relief. Thus, soil scientists proposed some applications to model cracks. The bulk apparent electrical conductivity of the soil is a useful measurement that is commonly used to map the spatial variability of soil salinity, water content, and clay content, especially as they relate to agriculture and land management. It can be used as a proximal sensing tool to map changes in cracking potential across these landscapes. These maps will be useful for predicting soil cracking potential in spatially distributed hydrology models (Neely, Morgan, Hallmark, McInnes, & Molling, 2016). Experimental efforts are also applied to measure cracks propagation. Dr. Neely et

al. (2014) proposed an instrumentation to measure soil subsidence and water content in a single borehole to measure soil shrinkage with loss of water. It provides more accurate relationships between soil water loss and soil shrink-swell due to the elimination of horizontal variability. This method provides higher-quality data on in situ soil shrinkage, providing valuable information on the behavior of shrink-swell soils (Neely, Ackerson, Morgan, & McInnes, 2014).

Desiccation cracks also have engineering and geotechnical effects with potentially very serious environmental and public safety issues. For example, desiccation cracks may trigger the onset of a landslide because its development at the surface of a slope. If they develop in the core of an earth dam, cracks act as flow paths. This would increase the moisture content of the dam and the pore water pressure which eventually leads its failure.

Nowadays, computational techniques offer the ability to model the formation and propagation of cracks in several geo-mechanical problems based on the governing and constitutive equation that describe the interactions between solids and fluids. However, the modeling of this type of problem is very challenging. The mesh fragmentation technique (MFT) was recently developed (Sánchez et al., 2014) to simulate this type of problem. The numerical approach has been implemented in the finite element program CODE_BRIGHT and it has been applied to simulate synthetic and theoretical cases, but it has not been validated against field data yet. Thus, the field test results from Konrad (Konrad & Ayad, 1997) is used to validate our code.

1.2 Objectives

In this work, the cracks are modeled by considering finite elements with high aspect ratio, which are introduced between the bulk elements of the mesh during the pre-process. The soil behavior is mimic by using the Barcelona Basic Model (BBM). The MFT is very promising for THM (Thermal-hydro-mechanical) modeling of problems involving discontinuities. However, only fully coupled hydro-mechanical problem is considered in this research. Whatsmore, the MFT does not require the use of re-meshing algorithms or any kind of special integration scheme. Based on these features, the MFT can be adopted to represent desiccation cracks in soils, which strongly affect the permeability and strength, which may cause geotechnical problems in infrastructure and building.

Thus, the primary objectives of the proposed research are:

- Gain a better understanding of key concepts that influence the formation and propagation of discontinuities in geo-materials;
- Capture the key hydro-mechanical properties and features of the case study reported in Konrad and Ayad (1997) and incorporate them into a finite element model
- Develop an advanced model able to reproduce the main characteristics of the case under study with the aim of capturing the evolution and trends of main variables reported in Konrad and Ayad (1997), including cracks network characteristics.

1.3 Organization of this dissertation

In this dissertation, 7 chapters are introduced to explain basic theory and process of this research.

In Chapter 1, the motivation and objectives of the research were introduced. This part explains the influence of desiccation cracks on geotechnical engineering and agricultural. Some experiment efforts have been made to predict propagation of cracks and computation techniques are published to model the formation of cracks as well. This research uses the MFT to mimic cracks propagation in field test and several objectives are supposed to achieve in this research.

In Chapter 2, several publications are reviewed to introduce the theory of desiccation cracks. The mechanism of cracking and analytical solutions of depth of cracks are explained in this chapter. Experimental methods to capture propagation of cracks, as well as the numerical applications intended to capture cracks propagation in field are proposed in this chapter. Background of Damage model is introduced in this chapter as well because damage model is used to mimic cracks propagation in this research.

In Chapter 3, the theoretical formulations used in CODE_BRIGHT which is the FEM code we use in this research are described. Constitutive equations of hydraulic and mechanical are summarized. These equations connect different properties in hydraulic and mechanical properties.

In Chapter 4, the Mesh Fragmentation Technique and damage theory which is adopted in the high aspect ratio interface element are introduced. The IMPL-EX integration scheme is explained as well.

In Chapter 5, details of the field test in Konrad and Ayad (1997) are described. Instruments of the field test, crack propagation mechanism, hydraulic and mechanical properties of the clay deposit in the field are emphasized to validate the model. The mechanical properties of the clay deposit that may influence the model are explained in this chapter.

In Chapter 6, an advanced model is developed to capture the evolution and tendency of main features in field test. Matching results of hydraulic and mechanical properties and formation of cracks of the model are shown in this chapter. The proposed framework is able to approximately predict the formation of cracks.

Chapter 7 is a summary of the dissertation. Some improvements in future are mentioned as well.

2. LITERATURE REVIEW

2.1 Desiccation cracks

Even though the mechanisms of cracking are very complex, numerous publications have sought to find out what influence the formation of cracks. The tensile forces induced by drying shrinkage must exceed the tensile stress of the soil to crack. The suction may induce soil contraction and cracking, which leads to vertical cracks below horizontal drying surface. The depth of cracks increases because of the desiccation of the soil (Miller, Mi, & Yesiller, 1998). Towner (1987) find out the water content and corresponding suction would influence the tensile stress and the tensile strength. The change of soil-water suction for isotropic shrinkage directly connect to induced stress of shrinkage (Towner, 1987). Speed of desiccation influence cracks formation as well. Rapid desiccation creates more widely spaced cracks than those produced by slow desiccation. The composition of the soil affects spacing of cracks as well. Cracks polygons created in soil with addition of sand are much smaller than those formed in clay mud. Degree of salinity of water is another important factor. High degree of salinity delays the formation of drying cracks. It results in margins of crack polygons downward as well (Kindle, 1917).

Morris et al (1992) provide analytical solutions to predict the depth of cracks propagate based on suction distribution from ground surface to water table. The max suction was assumed at ground surface because of most evaporation while suction at water table was zero because it is fully saturated (Morris, Graham, & Williams, 1992). Fredlund and Rahardjo (1993) presented another analytical solution. It is a function of depth to water table, soil density, suction, Poisson's ratio, and soil elastic moduli. A linear suction profile from the water table to the ground surface is assumed (Fredlund, Rahardjo, & Fredlund, 1993). Kodikara et al illustrate a different analytical

solution to predict the maximum tensile stress. The tensile strength develops in a clay layer for a given reduction in moisture content. When maximum tensile stress exceeds the tensile strength of soil, cracks would be assumed to propagate through layers (Kodikara & Choi, 2006).

There is a large body of measurements from digitized images to quantify soil structure, and many corresponding papers were published in the last three decades (e.g, RINGROSE‐VOASE and BULLOCK 1984; Moran et al. 1994). Crack Intensity Factor (CIF) was introduced to explain geometric features of cracks, such as width, depth and surface area. CIF is defined as the time variable ratio of the surface crack surface area to the total surface area of the clay. Image processing with a computer is used to determine CIF values from scanned photos of desiccation procedures (Miller et al., 1998). Fig 1 illustrates formation of cracks captured by image processing method. But there are some limits for image processing experiment. These experiments are time-consuming and demanding testing time of weeks or longer; Complex requirements for measurement and control of suction in failure-based tests; Limits in the ranges of suction or hydraulic conductivity; Limits under drying condition; Limits to certain type of soils. To improve experiment method, the transient water release and imbibition (TWRI) method, was introduced by Wayllace and Lu (2012). The TWRI method addresses all four aforementioned limitations and combines a simple, fast, accurate water-content-change measurement for the SWRC, HCF, and SSCC of all types of soils under drying and wetting conditions (Lu, Şener-Kaya, Wayllace, & Godt, 2012). Besides, Lu (2013) proposed the drying cake method applied with the PIV technique (White et al., 2003) to acquire time-sequence displacement fields of a drying cake and a linear elasticity solution of the displacement field to infer suction stress as a function of drying cake's moisture content (Lu & Kaya, 2013). Fig 2 presents the procedure of PIV technique.

Even though field work provides reliable results to get soil properties and propagation of cracks, numerical modeling, which are needed in this research, are still important. In order to get more accurate results, many efforts to improve numerical methods of simulating drying cracks have been made.

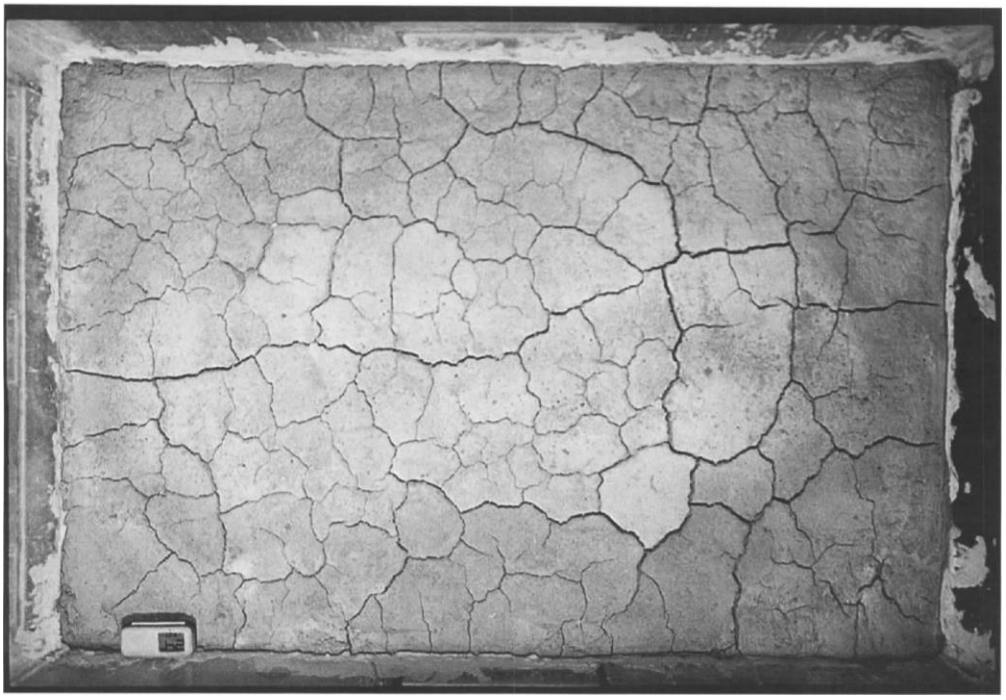

Figure 1. Cracks network captured by image processing method (reprinted from Miller et al., 1998)

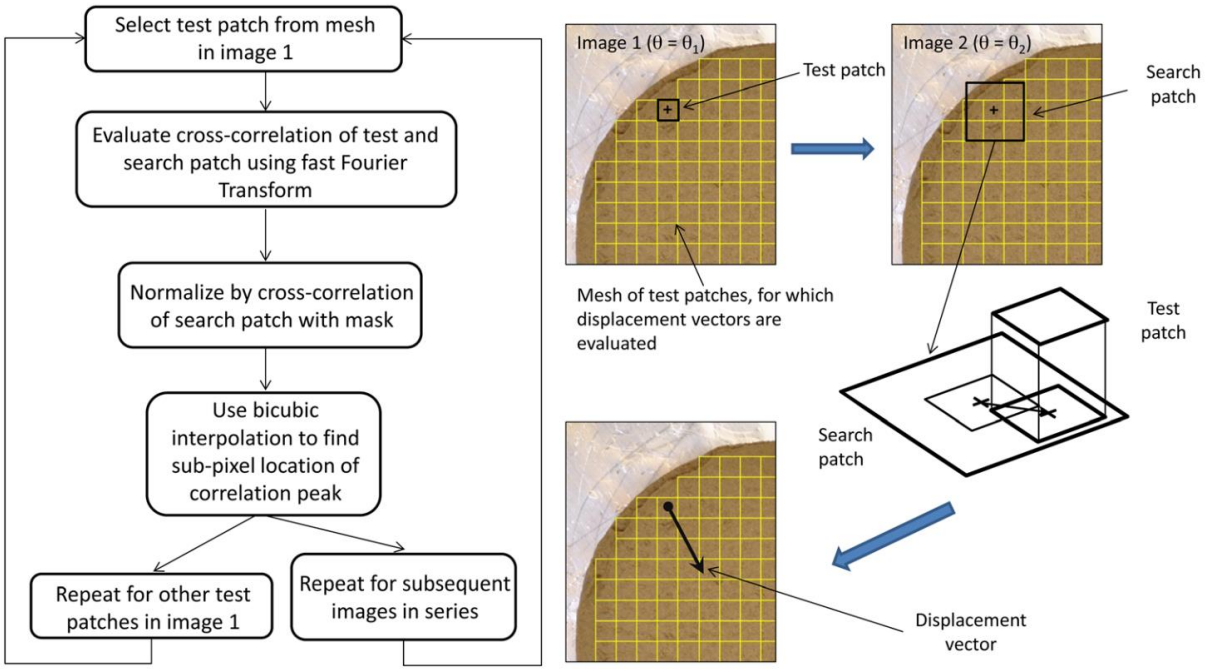

Figure 2. Illustrations of procedure of PIV technique (reprinted from Lu and Kaya, 2013)

2.2 Numerical modeling of desiccation cracks

The model to simulate damage and fracture of porous media has been proposed for years. The coefficient of linear extensibility (COLE) is one of model theories. It can be used to parameterize soil shrinkage models by defining the slope of vertical shrinkage with loss in water content (Kishné et al., 2009; Neely, 2014). It is interesting because it is different from finite element method, which is popular among engineers to do simulation. COLE combined mathematical thinking and experiment data base to predict soil shrinkage volume, on the other hand, soil cracks propagation. For finite element method, smeared cracking is adopted to represent cracks propagation based on stress strain relations in continuum mechanics approach (Cervera, Oliver, & Manzoli, 1996; Rots, Nauta, Kuster, & Blaauwendraad, 1985). However, the formation of macro-localized cracks cannot be simulated in the model and the simulation results tremendously depend on the mesh. On the other hand, discrete constitutive relationships between

stresses and relative displacement are suitable to capture the cracking process as well. The relationship is presented by the faces of adjacent finite elements (Hillerborg, Modéer, & Petersson, 1976). The interaction between these faces is established with constitutive model (Ingraffea & Saouma, 1985). As the crack propagation is unknown before the analysis, a remeshing strategy is required to adapt the discontinuity into the finite element mesh. To avoid this issue, embedded cracks are developed to capture the effects of crack (O. L. Manzoli & Shing, 2006; Moës & Belytschko, 2002; Moës, Dolbow, & Belytschko, 1999; Oliver, 1996; Simo, Oliver, & Armero, 1993).

Meakin (1987) propose a two-dimensional heterogeneous network, in which all the elements of the model have the same elastic behavior, but their breaking thresholds are randomly assigned. Each site of the system is connected by an elastic bond to a network where a uniform deformation is applied. All the coupling bond are identical to breaking (Meakin,1987). Colina et al. (1993) simplify the model by considering an electrical analog. Fig 3 presents the electrical analog model. The system is an L×L square lattice at 45 ° of electrical fuses having equal unit conductance and randomly assigned breaking threshold. The fuse network is coupled to the substrate by electrical resistors of conductance (Colina, De Arcangelis, & Roux, 1993). By inspiring by these two models, So Kitsunezaki (1999) proposed the thin-film model. Fig 4. Shows the thin-film model. The coating is a network of springs with elastic constants, forming a triangular lattice. The film is attached to the substrate elastically so that the surface layer can move relatively to the bulk. Each spring can break under stress (Kitsunezaki, 1999). These models are all based on elastic theory to simulate cracks.

Parks et al. (2008) proposed a different model based on Peridynamics (PD) which is a continuum theory that employs a nonlocal model to describe material properties. Nonlocal means

that continuum points separated by a finite distance may exert force upon each other (Parks, Lehoucq, Plimpton, & Silling, 2008). This model is interesting because models established before are based on "local force" which means that only continuum points in direct contact can exert a force on each other. But for PD theory, it is implemented with "nonlocal force" which is defined by generalizing the local force assumption to allow force at a distance. Jabakhanji et al. (2015) present a peridynamic model for transient moisture flow in unsaturated, heterogeneous, and anisotropic soils. Fig 5. clarify the peridynamic medium. Point **x** is influenced by all points within its horizon. $\mathcal{H}_x$ is the horizon of **x**, and δ is radius of the horizon. The model is an alternative to the classic Richard's equation and is based on Silling's reformulation of the theory of elasticity for solid mechanics. The flow is driven by the hydraulic potential field instead of the gradient of the hydraulic potential field (Jabakhanji & Mohtar, 2015).

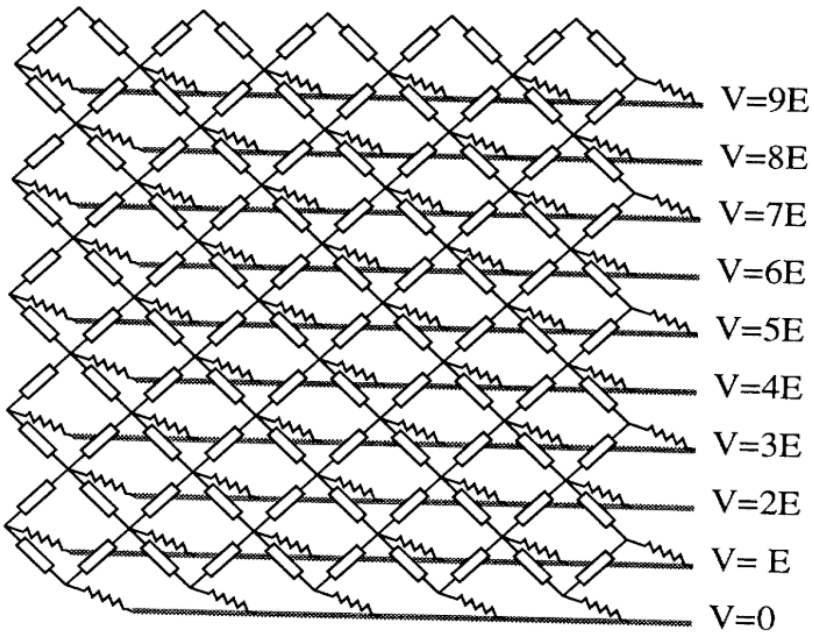

Figure 3. Electrical analog model coupled by two-dimensional lattice of fuses (reprinted from Colina, De Arcangelis, & Roux, 1993)

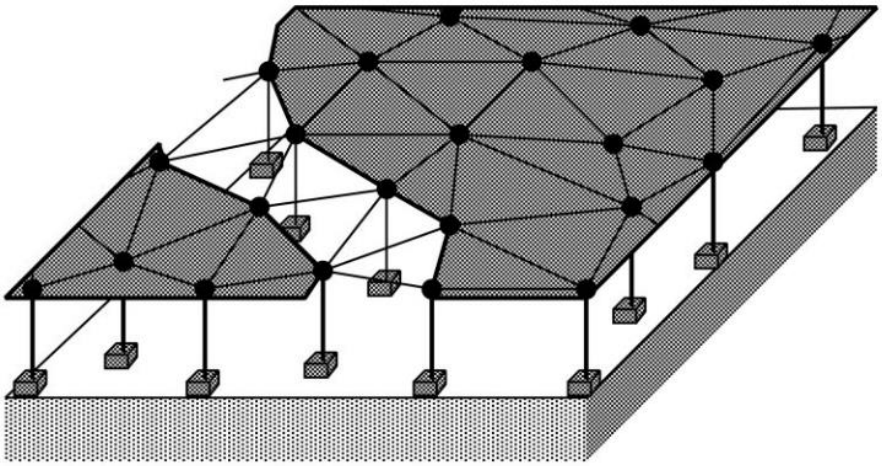

Figure 4. The two dimensional thin-film model. Blank triangular represents cracks (reprinted from Kitsunezaki, 1999)

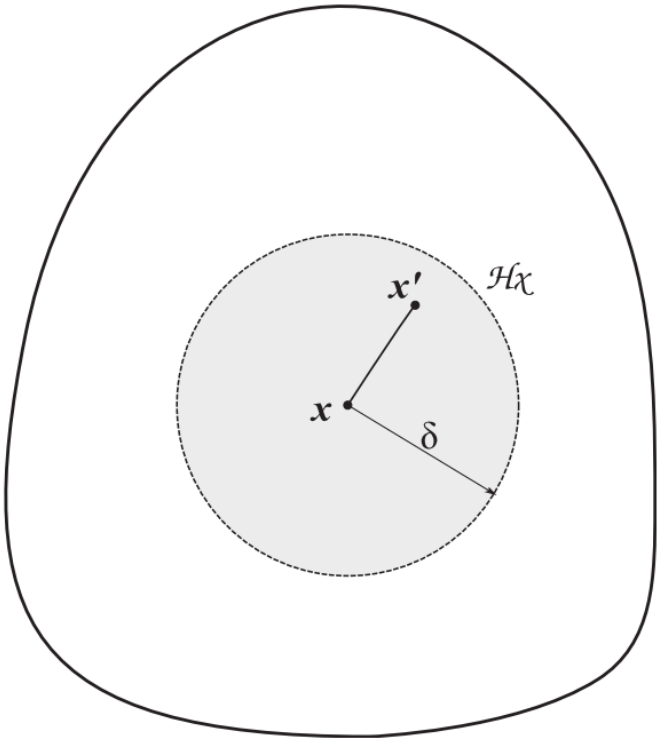

Figure 5. Illustration of peridynamic medium (reprinted from Jabakhanji & Mohtar, 2015)

2.3 Damage model

Even though drying cracks is a very common phenomenon in geotechnical engineering, most work of crack mechanism is applied in structure engineering. Damage model used in this research is developed in structural engineering. The internal damage can be connected as the presence and evolution of microscopic voids and this may eventually lead to cracks. In many engineering problems, cracks influence service life of engineering material and may trigger significantly problems like landslide or collapse of earth dam. In a number of practical situations, the ignorance of material degradation leads to consequences that are related to economic losses.

The cracking process changes the elastic properties of the material and decreases its effective area. This loss of effective area gradually increases because of voids. Even though damage and plasticity are complementary phenomena, cold material can fracture even before it reaches plastic mechanisms (Oller, Oñate, Oliver, & Lubliner, 1990). When material is subjected to loading cycle, the damage can be influence by shape fatigue as well. When metal experience high temperature, it may also make metal in viscous plastic deformations. Thus, the damage is not only on the nature of the material, but also on the type of loading and temperature (Jean Lemaitre, 1992). The concepts of mechanics of continuous medium allowed the development of constitutive equations which is able to model the evolution of cracks. This is known as Continuous Damping Mechanism (MDC). Theories of continuous damage are based on irreversible thermodynamic processes and the state of the internal variable (Simo & Ju, 1987).

3. HM THEORETICAL FORMULATION

A complete description of the THM formulation adopted for the analysis is presented in Olivella et al., 1994 (Olivella, Carrera, Gens, & Alonso, 1994), only a brief description is included here. This formulation considers the main thermal, hydraulic and mechanical phenomena. The problem is approached using a multiphase, multi species formulation that expresses mathematically the main THM phenomena in terms of the governing equations that can be divided into three groups: balance equations, constitutive equations and equilibrium restrictions. In this research, temperature is not considered. Only hydraulic and mechanical properties are observed.

3.1 Balance equations

The compositional approach has been adopted to establish the mass balance equations. This approach consists of balancing the species (mineral, water and air) rather than the phases (solid, liquid and gas) as Figure 6 shows. In the notation, the subscript is used to identify the phase (s for solid, l for liquid and g for gas) and the superscript to indicate the specie (w for water and a for air).

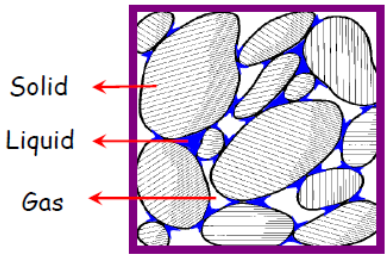

Figure 6. Scheme representation of the phases in the porous medium.

3.1.1 Solid mass balance equation

The balance of the solid phase can be expressed as:

$$\frac{\partial}{\partial t}\left(\theta_s\left(1-n\right)\right)+\nabla\cdot\left(\mathbf{j}_s\right)=0 \tag{3.1}$$

where θ_s is the mass of solid per unit volume of solid and $\mathbf{j}_s$ is the flux of solid. From this equation, an expression for porosity variation was obtained as:

$$\frac{D_s n}{Dt}=\frac{1}{\theta_s}\left[(1-n)\frac{D_s\theta_s}{Dt}\right]+(1-n)\nabla\cdot\frac{d\mathbf{u}}{dt} \tag{3.2}$$

The equation above has been developed using the material derivative with respect to the solid that can be defined as:

$$\frac{D_s\left(\bullet\right)}{Dt}=\frac{\partial}{\partial t}+\frac{d\mathbf{u}}{dt}\cdot\nabla\left(\bullet\right) \tag{3.3}$$

Equation (3.3) expresses the variation of porosity caused by volumetric deformation and solid density variation.

3.1.2 Water mass balance equation

Under unsaturated conditions, water is present in two phases: liquid and gas. The total mass balance can be written as:

$$\frac{\partial}{\partial t}\left(\theta_l^w S_l n+\theta_g^w S_g n\right)+\nabla\cdot\left(\mathbf{j}_l^w+\mathbf{j}_g^w\right)=f^w \tag{3.4}$$

where f_w is an external supply of water. An internal production term is not included because the total mass balance inside the medium is performed. The use of the material derivative leads to:

$$n\frac{D_s\left(\theta_l^w S_l+\theta_g^w S_g\right)}{Dt}+\left(\theta_l^w S_l+\theta_g^w S_g\right)\frac{D_s n}{Dt}+\left(\left(\theta_l^w S_l+\theta_g^w S_g\right)n\right)\nabla\cdot\frac{d\mathbf{u}}{dt}+\nabla\cdot\left(\mathbf{j}'^w_l+\mathbf{j}'^w_g\right)=f^w \tag{3.5}$$

3.1.3 Air mass balance equation

Once the other mass balance equations have been written, it is straightforward to obtain the mass balance of air taking into account that air is the main component of the gas phase and that it may be also present as dissolved in air in the liquid phase.

$$n\frac{D_s\left(\theta_l^a S_l+\theta_g^a S_g\right)}{Dt}+\left(\theta_l^a S_l+\theta_g^a S_g\right)\frac{D_s n}{Dt}+\left(\left(\theta_l^a S_l+\theta_g^a S_g\right)n\right)\nabla\cdot\frac{d\mathbf{u}}{dt}+\nabla\cdot\left(\mathbf{j}_l^{'a}+\mathbf{j}_g^{'a}\right)=f^a \tag{3.6}$$

3.1.4 Momentum balance equation

If the inertial terms are neglected, the momentum balance equation reduces to the equilibrium of stresses:

$$\nabla\cdot\sigma+\mathbf{b}=\mathbf{0} \tag{3.7}$$

where σ is the stress tensor and b is the vector of body forces.

3.2 Constitutive equations

The constitutive equations establish the link between the independent variables (or unknowns) and the dependent variables. There are several categories of dependent variables depending on the complexity with which they are related to the unknowns. The governing equations are finally written in terms of the unknowns when the constitutive equations are substituted in the balance equations. The constitutive equations for the thermal, hydraulic and mechanical problem are presented next.

3.2.1 Hydraulic

Regarding the hydraulic problem, the general Darcy's law can relate the unsaturated flow with the fluid pressures with the following expression:

$$\mathbf{q}_\alpha = -\mathbf{K}_\alpha \left(\nabla P_\alpha - \rho_\alpha \mathbf{g} \right) \tag{3.8}$$

where the subscript α refers to the phase as $\alpha = \mathrm{l}$ for the liquid phase and $\alpha = \mathrm{g}$ for the gas phase. P_α is the phase pressure, ρ_α is the phase density and g is the gravity vector. $\boldsymbol{K}_\alpha$ is the permeability tensor that depends on fluid viscosity, degree of saturation and pore structure. The permeability tensor is not constant. However, it depends on other variables:

$$\mathbf{K}_\alpha = \mathbf{k} \frac{k_{r\alpha}}{\mu_\alpha} \tag{3.9}$$

where k is the intrinsic permeability tensor, and kr□ are the dynamic viscosity and relative permeability of the phase, respectively.

The intrinsic permeability depends on the pore structure. This dependence is considered in terms of porosity. Two laws are being used in the analysis. In the first law, the intrinsic permeability of the bentonite is a function of the porosity:

$$\mathbf{k} = k_0 \frac{n^3}{\left(1-n\right)^2} \frac{\left(1-n_0\right)^2}{n_0^3} \mathbf{I} \tag{3.10}$$

where k_0 is the reference permeability at the reference porosity n_0. The second approach corresponds to an exponential law, presented as follows:

$$\mathbf{k} = k_0 \exp[b\left(n-n_0\right)]\mathbf{I} \tag{3.11}$$

where k_0 is the intrinsic permeability for a reference porosity n_0, b is a model parameter and I is the identity tensor. The model parameters (k0 = 5.0 x 10-20 m2; n0 = 0.14 and b = 50) have been determined from back calculations of the results of permeability tests under isochoric conditions (Figure 7).

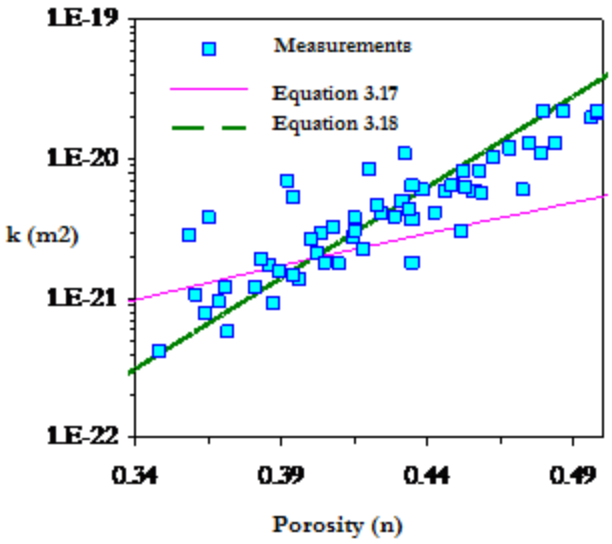

Figure 7. Variation of saturated permeability with porosity. Experimental data and adopted models for the intrinsic permeability law

The relative permeabilities for the liquid and gas phase depend on the degree of saturation and can be expressed as:

$$a)\ k_{rl} = S_{el}^{\ n} \qquad b)\ k_{rg} = \left(1 - k_{rl}\right) \tag{3.12}$$

where:

$$S_{el} = \frac{S_l - S_{lr}}{S_{ls} - S_{lr}} \tag{3.13}$$

S_{lr} , S_{ls} and n are model parameters. Equation (3.13) considers the decrease in hydraulic permeability as the degree of saturation decreases. This variation is very difficult to determine directly and it is necessary to resort to indirect ways of estimation.

To establish the link between the degree of saturation and suction, the retention curve (Figure 8) was used with the following expression:

$$S_{el} = \left[1 + \left(\frac{s}{P_o}\right)^{\frac{1}{1-\lambda_o}}\right]^{-\lambda_o} f_d \tag{3.14}$$

$$f_d = \left(1 - \frac{s}{P_d}\right)^{\lambda_d} \tag{3.15}$$

where s is the suction, P_o is the air entry value and λ_o is a model parameter. The function f_d is used to obtain more reasonable values at high suctions.

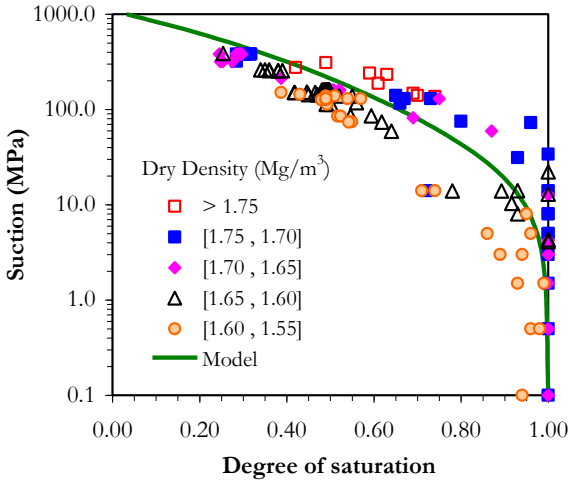

Figure 8. Retention curve adopted in the analyses, together with the experimental data of FEBEX bentonite (symbols)

The Fick's law has been used to explain the diffusion process occurring in the system. This law describes the water vapor diffusion in the gas phase and air diffusion in water. In addition, with this expression the non-advective fluxes of species inside the fluid phases can be computed. It also expresses them in terms of gradients of mass fraction of species through a hydrodynamic dispersion tensor that includes both molecular diffusion and mechanical dispersion (Antonio Gens, 2000; Olivella et al., 1994):

$$\mathbf{i}_\alpha^i = -\mathbf{D}_\alpha^i \nabla \omega_\alpha^i \qquad i = w, a; \qquad \alpha = l, g \tag{3.16}$$

where Di is the dispersion tensor of the medium.

For vapor diffusion, the following expression for the hydrodynamic dispersion tensor is adopted (Olivella et al., 1994):

$$\mathbf{i}_g^w = -\mathbf{D}_g^w \nabla \omega_g^w = -\left(n \rho_g S_g \tau D_m^w \mathbf{I} + \rho_g \mathbf{D}_g^{'} \right) \nabla \omega_g^w \tag{3.17}$$

where D_g^w is the dispersion tensor, τ is the tortuosity, D_m^w is the dispersion coefficient corresponding to molecular diffusion of vapor in air and D_g' is the mechanical dispersion tensor. The molecular diffusion coefficient is given by (Antonio Gens, 2000; Olivella et al., 1994):

$$D_m^w = 5.9x10^{-12} \frac{\left(273.15 + T\right)^{23}}{P_g} \tag{3.18}$$

where D_m^w is in m2/s, Pg is in MPa and T in ºC.

The mechanical dispersion can be defined with the following expression(Antonio Gens, 2000; Olivella et al., 1994):

$$\mathbf{D}_g^{'} = -\mathbf{q}_g \mathbf{I} + \left(d_l - d_t \right) \frac{\mathbf{q}_g \mathbf{q}_g^t}{\left| \mathbf{q}_g \right|} \tag{3.19}$$

where dt and dl are the transversal and longitudinal dispersivities, respectively.

Finally, the diffusion of air in the liquid phase can be written as:

$$\mathbf{i}_l^a = -\mathbf{D}_l^a \nabla \omega_l^a = -\left(n \rho_l S_l \tau D_m^a \mathbf{I} + \rho_l \mathbf{D}_l^{'} \right) \nabla \omega_l^a \tag{3.20}$$

3.2.2 Mechanical

The mechanical constitutive law adopted is the Barcelona Basic Model (BBM). The BBM is an elasto-plastic strain hardening model which extends the concept of critical state for saturated soils to unsaturated conditions and it is capable to reproduce the behavior observed under these conditions. This model takes into account two independent stress variables: the net stress (σ), defined as the excess of the total stresses over the gas pressure ($\sigma_t - \boldsymbol{I} p_g$) and the matric suction (s), defined as the difference between gas pressure and liquid pressure. The BBM was created in

terms of the three stress invariants (p, J, θ), suction and temperature. The stress invariants are defined as follows:

$$p = \left(\frac{1}{3}\right)\left(\sigma_x + \sigma_y + \sigma_z\right) \tag{3.21}$$

$$J^2 = \frac{1}{2trace\left(s^2\right)} \tag{3.22}$$

$$\theta = -\frac{1}{3}\sin^{-1}\left(1.5\sqrt{3}\det s / J^3\right) \tag{3.23}$$

$$s = \sigma - pI \tag{3.24}$$

where ***I*** is the identity tensor. In this model the yield surface depends also on the matric suction. The trace of the yielding function on the p-s plane is called the LC (Loading-Collapse) curve. This curve represents the position where the activation of permanent deformations due to loading increments or wetting takes place. The position of the LC curve is given by p_0^*, the pre consolidation yield stress for saturated conditions. Preconsolidation pressure is affected by the temperature assuming that temperature increases reduce the size of the yielding surface and the strength of the material. This is a common behavior for saturated soils as established in Hueckel and Borsetto, (1990) (Hueckel & Borsetto, 1990) and can also be extended to unsaturated conditions as recent experimental studies show. The BBM yield surface can be expressed as:

$$F_{LC} = 3J^2 - \left[\frac{g(\theta)}{g\left(-30^\circ\right)}\right]^2 M^2\left(p + p_s\right)\left(p_0 - p\right) = 0 \tag{3.25}$$

where M is the slope of the critical state, p_0 is the unsaturated isotropic pre consolidation stress at a specific value of suction and p_s takes into account the dependence of shear strength on suction

and temperature. In addition, $g(\theta)$ represents the Lode's angle function. When yielding takes place, the increment of plastic deformation is defined as:

$$\varepsilon_{LC}^{\dot{p}} = \lambda_{LC} \frac{\partial G}{\partial \sigma} \tag{3.26}$$

where λ_{LC} is the plastic multiplier and G is the plastic potential determined as follows:

$$G = \alpha_G 3J^2 - \left[\frac{g(\theta)}{g(-30^\circ)}\right]^2 M^2 (p + p_s)(p_0 - p) = 0 \tag{3.27}$$

α_G is determined according to (Alonso, Gens, & Josa, 1990).

The hardening law is expressed as a rate relation between the volumetric plastic strain and the saturated isotropic pre consolidation stress p_0^* according to:

$$\frac{\dot{p}_0^*}{p_0^*} = \frac{(1+e)}{(\lambda_{(0)} - \kappa)} \varepsilon_v^{\dot{p}} \tag{3.28}$$

where e is the void ratio, ε_v^p is the volumetric plastic strain, κ is the elastic compression index for changes in p and $\lambda_{(0)}$ is the stiffness parameter for changes in p for virgin states of the soil in saturated condition.

Due to the high compaction to which the bentonite has been subjected, the description of the behavior of the material inside the yield surface is relevant. According to the model parameters, it is expected that the stress path will lie inside the BBM yield surface. The variation of stress-stiffness with suction and the variation of swelling with stress and suction have been taken into account. The elastic model can be expressed as follows:

$$\dot{\varepsilon}_v^e = \frac{\kappa}{(1+e)} \frac{\dot{p}}{p} + \frac{\kappa_s}{(1+e)} \frac{\dot{s}}{(s+0.1)} + (\alpha_0 + \alpha_2 \Delta T)\dot{T} \tag{3.29}$$

$$\dot{\varepsilon}_s^e = \frac{J}{G_t} \tag{3.30}$$

where κ_s is the macrostructural elastic stiffness parameter for changes in suction, G_t is the shear modulus; α_0 and α_2 are model parameters related to temperature. κ, κ_s and G_t can be determined according to:

$$\kappa = \kappa_i \left(1+\alpha_s s\right) \tag{3.31}$$

$$\kappa_s = \kappa_{s0} \left(1+\alpha_{sp} \ln p/p_{ref}\right) \tag{3.32}$$

$$G_t = \frac{3\left(1-2\mu\right)K}{2\left(1+\mu\right)} \tag{3.33}$$

where μ is the Poisson's coefficient, α_s and α_{sp} are model parameters and K is the bulk modulus.

3.3 Equilibrium restrictions

Another type of relationships that relate dependent variables with unknowns are the equilibrium restrictions. They are obtained assuming chemical equilibrium for dissolution of the different species (air and vapor) in phases (liquid, gas).

The vapor concentration in the gaseous phase is governed by the psychometric law, which can be defined as (Antonio Gens, 2000):

$$\theta_g^w = \left(\theta_g^w\right)^0 \exp\left(\frac{\Psi M_w}{R\left(273.15+T\right)\rho_l}\right) \tag{3.34}$$

where θ_g^w is the vapor concentration in the gas phase; $(\theta_g^w)^0$ is the vapor concentration in the gas phase in equilibrium with a liquid at the sample temperature; Ψ is the total water potential of the water, in this case it is related to suction (Ψ = Pl - Pg); Mw is the molecular mass of the water (0.018 kg/mol) and R the gas constant (8.314 J/mol/ºK). The gases law relates vapor density and vapor pressure (Olivella et al., 1994):

$$\left(\theta_g^w\right)^0 = \frac{M_w P_{v(T)}}{R\left(273.15+T\right)} \tag{3.35}$$

For pure water, the vapor pressure has been approximate as (Olivella et al., 1994):

$$P_{v(T)} = 136075 \exp\left(\frac{-5239.7}{273.15 + T}\right) \tag{3.36}$$

To define the amount of air dissolved in water, Henry's law is adopted. This law expresses a linear relationship between the concentration of air in dissolution and the partial pressure of air (Pa) in the gaseous phase:

$$\theta_l^a = \omega_a^l \rho_l = \frac{P_a}{H} \frac{M_a}{M_w} \rho_l \tag{3.37}$$

where Ma is the molecular mass of the air (0.02895 kg/mol), and H is Henry's constant (1000 MPa).

4. MESH FRAGMENTATION TECHNIQUE AND DAMAGE THEORY

4.1 Mesh fragmentation process

The mesh fragmentation technique was proposed by Sanchez et al., (2014) for modeling the process of crack formation and propagation in soils during drying. It was used by Manzoli et al (2018) (O. Manzoli, Sánchez, Maedo, Hajjat, & Guimarães, 2018) to model drying in soils using orthotropic mechanical models. Fig. 9 illustrates the main steps involved in the mesh fragmentation techniques for 2D problems which can be summarized as follows:

1. Generation of the standard finite element mesh.
2. Separation of the regular finite elements (bulk elements) by inserting gaps between them.
3. Introduction of interface high aspect ratio finite elements (HAR-FE) in between the bulk finite elements of the original mesh.

It is significant to note that the gaps in Fig. 9 are illustrated in exaggerated scale. The gaps are actually very small. As it has been pointed out by Manzoli et al. (O. L. Manzoli, Maedo, Bitencourt, & Rodrigues, 2016), a ratio of 1% between the size of the smallest bulk element and the HAR-FE thickness may be considered. 1% of the typical size of the regular elements seems to be a very reasonable recommendation, because the size of the regular elements has been chosen to accurately capture the stress field prior to the crack formation. (O. L. Manzoli et al., 2016)

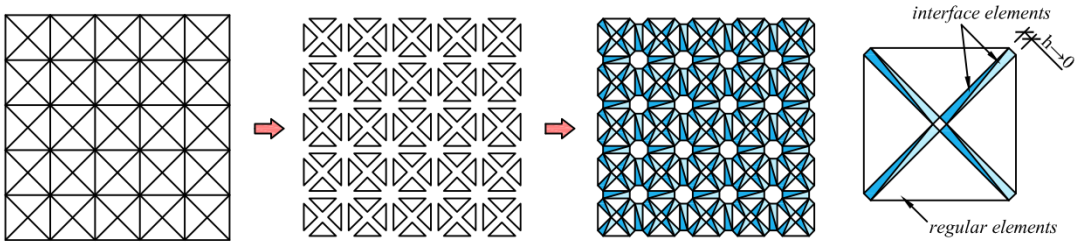

Figure 9. 2D mesh fragmentation process (reprinted from O.L. Manzoli et al., 2016)

4.2 Damage theory

4.2.1 Damage variable

For the one-dimensional and homogenous case, the damage is calculated on the basis of the reduction of cross-sectional area. Damage variable (d) is a variable to measure the level of damage. The definition of damage variable is given by:

$$\mathrm{d} = \frac{A_D}{A} \tag{4.1}$$

where A_D is area of damage and A is total cross-sectional area (Fig 10). There is a range for damage variable which is [0,1]. If damage variable is 0, it means no damage exists in this cross-sectional area (i.e., the material is intact) while 1 means the material is fully degraded.

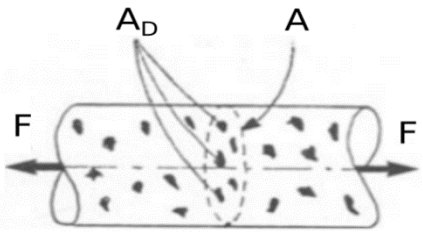

Figure 10. Fracture body (reprinted from Lemaitre, 1996)

4.2.2 Elastic stress

To clarify at first, the definition of elastic stress is based on structural engineering, which is extended to geotechnical engineering recently. The elastic stress is associated with effective area while total force is being applied to the total area of cross section. Thus,

$$\sigma = \frac{F}{A} \tag{4.2}$$

and

$$\overline{\sigma} = \frac{F}{\bar{A}} \tag{4.3}$$

where the effective area is expressed as,

$$\bar{A} = A - A_D \tag{4.4}$$

Similarly,

$$\frac{\sigma}{\bar{\sigma}} = \frac{\bar{A}}{A} = \frac{A - A_D}{A} = 1 - d \tag{4.5}$$

Thus,

$$\sigma = (1 - \mathrm{d})\bar{\sigma} \tag{4.6}$$

Equation (4.6) represents the relationship between the total stress and effective stress based on the damage level. It is clear from this equation that $\sigma = \bar{\sigma}$ when material is in its original state (i.e., $d = 0$). On the other hand, $\sigma = 0$ when the material is completely degraded. This makes sense because there would be no stress if material is totally damaged.

4.2.3 Hypothesis of strain equivalence

Based on the hypothesis of the equivalence of deformation (J. Lemaitre, 1984), the deformation of cracked material is calculated by the stress applied to the material. Fig 11 illustrates the deformation of different material. According to the hypothesis mentioned above, deformation of damage material and intact material can be written as

$$\varepsilon_1 = \varepsilon = \frac{\sigma}{E_D} \tag{4.7}$$

$$\varepsilon_2 = \varepsilon = \frac{\bar{\sigma}}{E} \tag{4.8}$$

where ε_1 is the deformation of damaged material, E_D is damaged young modulus, ε_2 is the deformation of whole material where E is intact young modulus. It is possible to establish a relationship between damaged and intact young moduli. The relationship can be written as follows,

$$\varepsilon = \varepsilon_1 = \varepsilon_2 = \frac{\sigma}{E_D} = \frac{\bar{\sigma}}{E} \Rightarrow E_D = \frac{\sigma}{\bar{\sigma}} E \tag{4.9}$$

Substituting equation (4.5) into equation (4.9) gives

$$E_D = (1 - d)E \tag{4.10}$$

Based on relationship established above, it is possible to develop the concepts of damage criterion, explicit evolution for the damage variable, hardening/ softening law and Kuhn-Tucker relation. These are fundament of damage theory, which will be described in following sections.

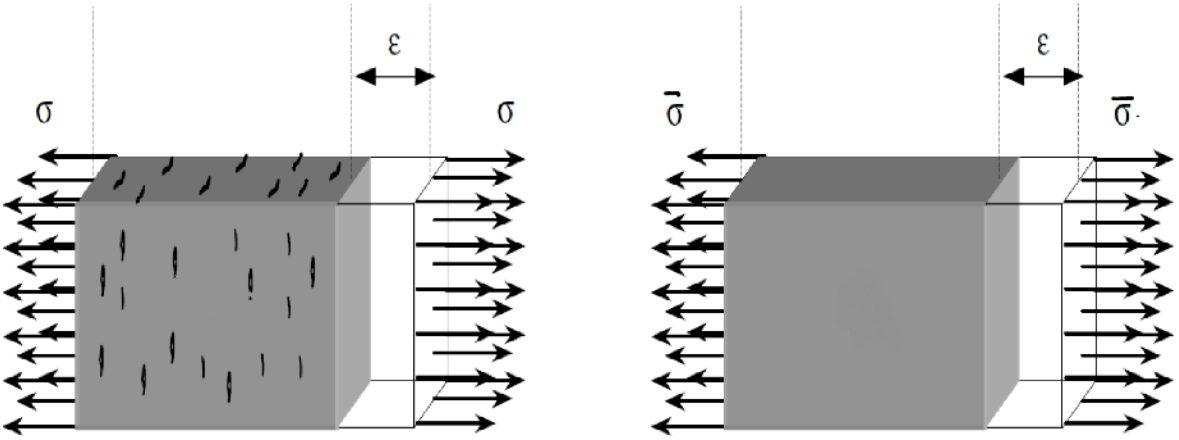

Damaged material Intact material

Figure 11. Material constitutive relation (reprinted from Oller 2001)

4.2.4 Damage Criterion

The damage criterion (ϕ) establishes the limits in which the solid behaves as an elastic material. It represents the process of degradation of material. In other words, it illustrates limits of elastic domain.

$$\phi(\sigma) = \tau - q \leq 0 \tag{4.11}$$

where q is sa tress-like internal variable which establish the size of domain and τ is the equivalent stress. Fig 12. shows some examples of damage criteria for one-dimensional problems.

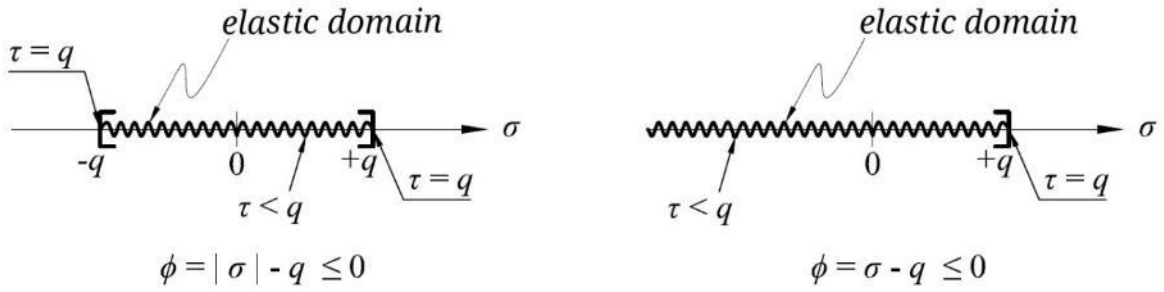

Figure 12. Illustration of damage criterion in one dimension (reprinted from Maedo, Manzoli, & Rodrigues, 2014)

The damage criterion can be rewritten in terms of effective stress as following,

$$\bar{\phi}(\bar{\sigma}) = \bar{\tau} - r \leq 0 \tag{4.12}$$

where $r = q/(1-d)$ is strain-like internal variable, which is always increasing, and its tangent will never be smaller than zero.

4.2.5 Explicit evolution for the strain like internal variable

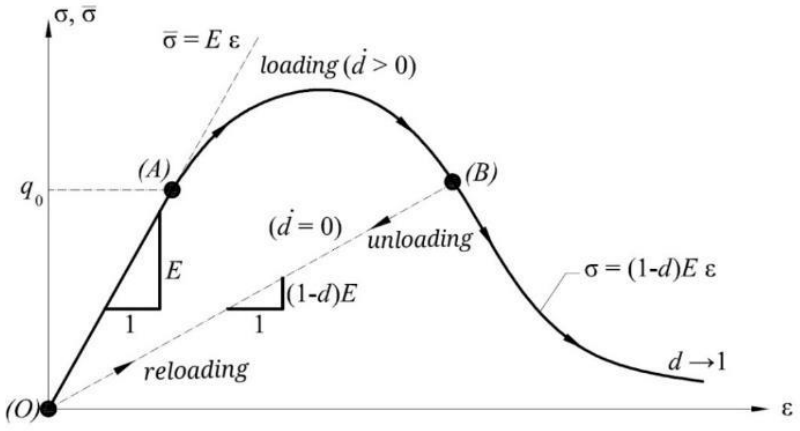

Figure 13. Diagram of axial strain

Fig 13. Illustrates the relationship of stress and strain in a whole loading cycle. As we can see, this material exhibits a linear elastic behavior at initial stage (OA), which means no damage occurs in this stage and $\dot{d}$ =0, $\bar{\phi} < 0$. After stage of OA, irreversible damage starts to occur in OB stage, which means $\dot{d} > 0$, $\bar{\phi} = 0$. $\bar{\phi} = 0$ because it reaches the damage criterion. Thus, Kuhn-Tucker relations can be concluded as following,

$$\dot{d}\bar{\phi} = 0, \dot{d} \geq 0, \bar{\phi} \leq 0 \tag{4.13}$$

When in loading plastic stage (AB), we can conclude following relationship based on definition of effective damage criterion,

$$\begin{cases} \dot{r} = \dot{\bar{\tau}} > 0 \\ \dot{d} > 0 \end{cases} \tag{4.14}$$

Equation (4.14) defines the evolution of the strain-like internal variable. When in unloading or reloading stage (OB), $\dot{\bar{\phi}} < 0$ because ofno evolution of elastic damage. Thus, following relationship can be included,

$$\begin{cases} \dot{r} = 0 \\ \dot{d} = 0 \end{cases} \tag{4.15}$$

In conclusion,

$$\text{If } \bar{\phi} < 0 \Rightarrow \dot{d} = 0$$

$$\text{If } \bar{\phi} = 0 \Rightarrow \begin{cases} \dot{\tau} < 0 & \begin{cases} \dot{r} = 0 \\ \dot{d} = 0 \end{cases} \\ \dot{\tau} > 0 & \begin{cases} \dot{r} > 0 \\ \dot{d} > 0 \end{cases} \end{cases}$$

Since $\mathrm{r} = q_0$ at initial stage and considering the Kuhn-Tucker loading-unloading relation, the evolution of the strain-like internal variable can be expressed as follows

$$\mathrm{r(t)} = \max_{s \in [0,t]} [q_0, \bar{\tau}(\mathrm{t})] \tag{4.16}$$

This means the internal strain variable equals the maximum stress value reached in the loading process.

4.2.6 Softening law and fracture energy

In this work, the softening law is described by an exponential function given by:

$$\mathrm{q(r)} = q_0 \exp\left[A\left(1 - \frac{r}{r_0}\right)\right] \tag{4.17}$$

where A is the softening parameter related to the fracture energy.

Table 1 contains all the ingredients needed for the continuum tensile damage model.

In order to define fracture energy in model I, let us assume a continuous body submitted to a force (**F**), as shown in Figure 14. The constitutive relation in this case is,

$$\dot{\varepsilon} = \frac{\dot{\bar{\sigma}}}{E} > 0 \;\Rightarrow \dot{\bar{\sigma}} = E\dot{\varepsilon} > 0 \tag{4.18}$$

$$\dot{r} > 0 \;\Rightarrow\; \dot{\bar{\phi}} = \dot{\bar{\tau}} - \dot{r} = 0 \Rightarrow \dot{\bar{\tau}} = \dot{r} \tag{4.19}$$

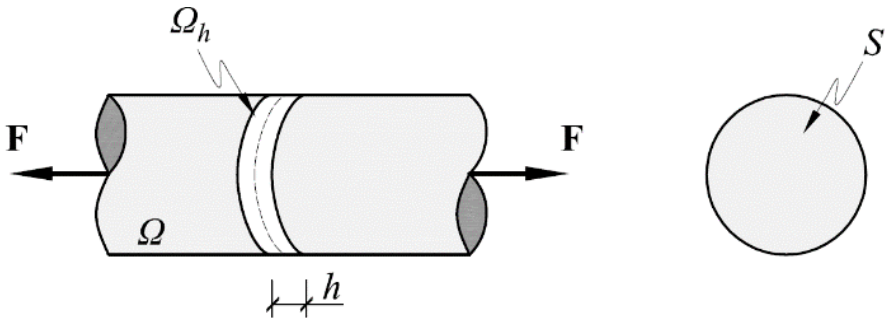

Figure 14. Solid body under continuous force (reprinted from Maedo 2015)

According to equation (4.18) and (4.19), equation (4.20) can be captured,

$$\dot{\bar{\sigma}} = \dot{\bar{r}} = E\dot{\varepsilon} \;\Rightarrow \dot{\varepsilon} = \frac{\dot{r}}{E} \tag{4.20}$$

Considering a region $(\mathrm{d}\Omega)$ of localized deformation zone with cross section S and thickness h, one can write

$$\mathrm{d}\Omega = \mathrm{h}\mathrm{d}S \tag{4.21}$$

Assuming the application of a monotonic load, the external power can be described by the integration of the strain energy in the body,

$$p_{ext}^{\Omega} = \int_{\Omega} \sigma \dot{\varepsilon} d\Omega = \int_{\Omega} \underbrace{(1-d)}_{\frac{q}{r}} \underbrace{E\varepsilon}_{r} \underbrace{\dot{\varepsilon}}_{\frac{\dot{r}}{E}} d\Omega = \int_{\Omega} q \frac{\dot{r}}{E} d\Omega = \int_{\Omega} q \frac{\dot{q}}{HE} d\Omega \tag{4.22}$$

where $H = q^{\cdot}/(r^{\cdot}) = -A \exp A(1 - r/r_0)$. Based on exponential law in equation (4.20), equation (4.22) can be rewritten as

$$p_{ext}^{\Omega} = \int_{\Omega} \frac{q_0 \, \dot{q}}{H \, E} d\Omega \tag{4.23}$$

According to equation (4.17), equation (4.23) is transferred to

$$p_{ext}^{\Omega} = -\int_{\Omega} q_0 \frac{\dot{q}}{AE} d\Omega \tag{4.24}$$

Taking equation (4.21) into consideration,

$$p_{ext}^{\Omega} = \int_{S} -q_0 \frac{\dot{q}}{AE} h dS = -\frac{q_0 h}{AE} \int_{S} \dot{q} dS \tag{4.25}$$

The cracking process of the material occurs in the time interval $\mathrm{t}\epsilon[0, t_{\infty}]$. Total work of cracking process is integration of external power input over time. Thus, total work can be calculated as,

$$W^{\Omega_h} = \int_0^{t_{\infty}} p_{ext}^{\Omega} \, dt = \int_0^{t_{\infty}} \left[-\frac{q_0 h}{AE} \int_{S} \dot{q} dS \right] dt \tag{4.26}$$

Applying Fubini's theorem, one can rewrite the previous equation as follows

$$W^{\Omega_h} = \int_S \left[\frac{q_0 h}{AE}\int_0^{t_\infty} \dot{q}\, dt\right] dS = \int_S \frac{h{q_0}^2}{AE} dS \tag{4.27}$$

where

$$G_f = h\frac{{q_0}^2}{AE} \tag{4.28}$$

is the fracture energy representing the energy spent in the form of a fracture per unit area. In this work, G_f is property of material associated with q_0, A and E.

Table 1. Summary of damage theory for 1D

Constitutive relation	$\sigma = (1-\mathrm{d})\bar{\sigma}$ $\bar{\sigma} = E\varepsilon$
Damage criterion	$\bar{\phi} = \bar{\tau} - r \le 0$
Evolution law for internal damage variable	$\mathrm{r(t)} = \max_{s\in[0,t]}[q_0, \bar{\tau}(\mathrm{t})]$
Damage evolution	$\mathrm{d} = 1 - \frac{q}{r}$
Hardening/Softening law	$\mathrm{q(r)} = q_0 \exp\left[A\left(1 - \frac{r}{r_0}\right)\right]$

4.2.7 Extension to 2D and 3D problem

The damage theory used in 1D problem can be extended to 2D and 3D problems. The 2D and 3D models are more complex because they required sophisticated operations. However, the main ingredients are very similar. In this section, the isotropic continuous damage model for multidimensional problems will be considered.

For 2D and 3D, second order tensors are adopted rather than scalar tensor. Thus,

$$\boldsymbol{\sigma} = (1 - \mathrm{d})\bar{\boldsymbol{\sigma}} \tag{4.29}$$

where the second order stress tensor is expressed by

$$\boldsymbol{\sigma} = \mathbf{C}\colon \boldsymbol{\varepsilon} \tag{4.30}$$

where **C** is a forth order elastic tensor and ε is strain tensor. The damage criterion can also be generalized for 2D and 3D analyses. Equation (4.31) exhibits the damage criterion in term of the elastic stresses,

$$\bar{\phi} = \tau(\bar{\boldsymbol{\sigma}}) - r \leq 0 \tag{4.31}$$

$$\tau(\bar{\boldsymbol{\sigma}}) = \bar{\sigma}_{nn} = \boldsymbol{n} \cdot \boldsymbol{\sigma} \cdot \boldsymbol{n} \tag{4.32}$$

where **n** is unit vector normal to the base of the HAR-FE and $\bar{\sigma}_{nn}$ is the component of the stress tensor that is normal to the base of the interface element.

The studies developed in this section illustrate the constitutive relations which can be used for the analysis of solid. They are the fundamental of CODE_BRIGHT which is used in this research.

Table 2. Equations for the continuum tensile damage model

Constitutive relation	$\boldsymbol{\sigma} = (1 - \mathrm{d})\bar{\boldsymbol{\sigma}}$ $\bar{\boldsymbol{\sigma}} = \mathbf{C}\colon \boldsymbol{\varepsilon}$
Damage criterion	$\bar{\phi} = \bar{\sigma}_{nn} - r \leq 0$
Evolution law for internal damage variable	$\mathrm{r(t)} = \max_{s\in[0,t]}[q_0, \bar{\sigma}_{nn}(\mathrm{t})]$
Damage evolution	$\mathrm{d} = 1 - \frac{q}{r}$
Hardening/Softening law	$\mathrm{q(r)} = q_0 \exp\left[A\left(1 - \frac{r}{r_0}\right)\right]$

4.3 High aspect ratio interface element

Since Barcelona basic model (BBM) is only for constitutive relation in soil, a damage model is required to capture propagation of cracks. High aspect ratio interface element is recently established to simulate propagation and formation of cracks (Marcelo Sánchez, Manzoli, & Guimarães, 2014b).

Let us consider the linear triangular element with base b and height h (Fig 15) so that h is the distance between node 1 and its projection on the base of the element. The strain tensor ($\boldsymbol{\epsilon}$) of this element can be split into two parts:

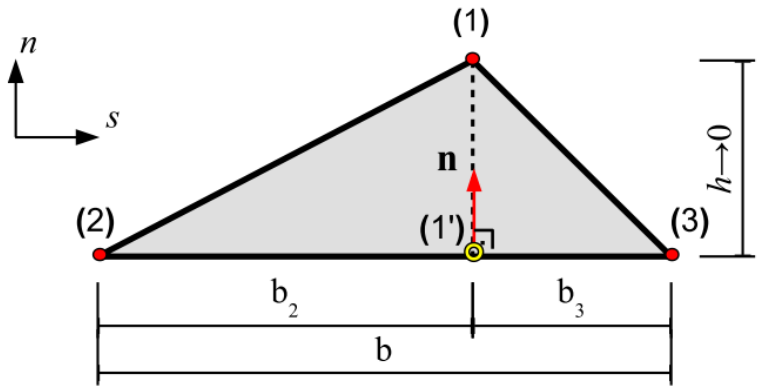

Figure 15. Three nodes solid interface element (reprinted from Manzoli et al 2014)

$$\boldsymbol{\epsilon} = \tilde{\boldsymbol{\epsilon}} + \hat{\boldsymbol{\epsilon}} \tag{4.33}$$

where $\hat{\boldsymbol{\epsilon}}$ corresponds to the tensor with components associated with the height h and $\tilde{\boldsymbol{\epsilon}}$ is the tensor containing the remaining terms. Therefore, equation (4.33) can be rewritten as

$$\boldsymbol{\epsilon} = \tilde{\boldsymbol{\epsilon}} - \underbrace{\frac{1}{h}(\boldsymbol{n} \otimes [\![\boldsymbol{u}]\!])^{S}}_{\hat{\boldsymbol{\epsilon}}} \tag{4.34}$$

where $(\cdot)^S$ denotes the symmetric part of the tensor in $(\cdot)$, $\boldsymbol{n}$ is the unit vector normal to the element base, $[\![\boldsymbol{u}]\!]$ is the relative displacement between node 1 and its projection on the base of the element and $\otimes$ is a dyadic product.

In the limit situation in which h tends to zero $(h \to 0)$, equation (4.34) is almost exclusively defined by the tensor $\hat{\boldsymbol{\epsilon}}$. In other words, the discontinuity of the linear triangular element with high aspect ratio can be expressed by the relative displacement between node 1 and its projection on the element base (1'). Hence, the relative displacement $[\![\boldsymbol{u}]\!]$ can be considered as the measurement of displacement discontinuity.

4.4 Discrete constitutive relation of interface element

The damage model explained before is adopted to represent the formation and propagation of cracks in solid materials. The present work uses the damage criterion based on the component of stress tensor which is normal to the base of the HAR-FE. Thus, the model is capable of mimic fracture in Mode I. Moreover, since the damage variable degrades all components of the elastic stress, it is also possible to reproduce the crack process in mixed mode.

In order to show that the stress-strain continuum constitutive relation tends to the discrete traction-separation relation as the aspect ratio increases, let us substitute equation (4.34) into equation (4.29),

$$\boldsymbol{\sigma} = (1-\mathrm{d})\mathbf{C}:\boldsymbol{\varepsilon} = (1-\mathrm{d})\mathbf{C}:\left[\frac{1}{h}(\boldsymbol{n}\otimes[\![\boldsymbol{u}]\!])^S + \tilde{\boldsymbol{\varepsilon}}\right] = \frac{(1-\mathrm{d})}{h}\mathbf{C}:[(\boldsymbol{n}\otimes[\![\boldsymbol{u}]\!])^S + \tilde{\boldsymbol{\varepsilon}}h] \quad (4.35)$$

When h tends to zero, equation (4.35) becomes the following cohesive law relating traction to discontinuity

$$\boldsymbol{t} = \boldsymbol{\sigma} \cdot \boldsymbol{n} = \underbrace{\frac{(1-\mathrm{d})}{h}}_{\widehat{\boldsymbol{K}}} (\mathbf{n} \cdot \mathbf{C} \cdot \mathbf{n}) \, [\![\boldsymbol{u}]\!]^S = \widehat{\boldsymbol{K}} [\![\boldsymbol{u}]\!] \tag{4.36}$$

The previous equation shows that the HAR-FE used in this work are able to emulate discrete cracks in solids by considering a continuum damage model.

4.5 IMPL-EX integration scheme

The Implicit-explicit integration scheme proposed by by Oliver et al. (2008) (Oliver, Huespe, & Cante, 2008) was used to compute the stresses from the damage model. This method is very robust, and it always converges with 2 Newton-Raphson iterations IMPL-EX algorithm addresses the update of the internal variable r to explain the limit of degradation. With the help of r value, the level of current damage and the tensor of current stresses can be obtained.

Table 2. shows the scheme for the implicit-explicit integration technique for equivalent stress $\bar{\tau} = \bar{\sigma}_{nn}$. This integration technique ensures convergence to the cost of a consistency violation. The algorithm may lose precision, and therefore, small load increments may be required in order to address this issue. The main advantage of this technique is its stability and computational robustness, because the IMPL-EX keep the convergence of every time step (Maedo et al., 2014).

Table 2. IMPL-EX integration scheme for damage model

Input: r_i, Δr_i, $\bar{\sigma}_{nn_{(i)}}$, $\varepsilon_{(i+1)}$

(1) Calculate the elastic stress tensor in step i+1:

$$\bar{\boldsymbol{\sigma}}_{(i+1)} = \boldsymbol{C}\colon \boldsymbol{\varepsilon}_{(i+1)}$$

(2) Calculate equivalent stress:

$$\bar{\tau}_{(i+1)} = \bar{\sigma}_{nn_{(i+1)}} = \boldsymbol{n} \cdot \bar{\boldsymbol{\sigma}}_{(i+1)} \cdot \boldsymbol{n}$$

(3) Verify the status of loading and unloading:

$$\text{If} \quad \bar{\sigma}_{nn_{(i+1)}} \leq r_i$$

$$\text{Then} \quad r_{(n+1)} = \bar{\tau}_{(i+1)}$$

$$\text{Else} \quad r_{(n+1)} = r_n$$

(4) Calculate the internal variable increment:

$$\Delta r_{(n+1)} = r_{(n+1)} - r_{(n)}$$

(5) Calculate the linear extrapolation of r:

$$\tilde{r}_{(i+1)} = r_{(i)} + \frac{\Delta t_{(i+1)}}{\Delta t_i}\, \Delta r_{(i)}$$

(6) Update the value of internal variable q based on exponential law and damage variable d

$$\tilde{q}_{(i+1)}(\tilde{r}) = q_0 \exp\left[A\left(1 - \frac{\tilde{r}_{(i+1)}}{q_0}\right)\right];\ \tilde{d}_{(i+1)} = 1 - \frac{\tilde{q}_{(i+1)}}{\tilde{r}_{(i+1)}}$$

(7) Update stress tensor:

$$\tilde{\boldsymbol{\sigma}}_{(i+1)} = \left(1 - \tilde{d}_{(i+1)}\right)\bar{\boldsymbol{\sigma}}_{(i+1)}, \ \text{if} \quad \bar{\sigma}_{nn_{(i)}} > 0$$

$$\tilde{\boldsymbol{\sigma}}_{(i+1)} = \bar{\boldsymbol{\sigma}}_{(i+1)}, \ \text{if} \ \ \bar{\sigma}_{nn_{(i)}} < 0$$

Output: $r_{(i+1)}$, $\Delta r_{(i+1)}$, $\bar{\sigma}_{nn_{(i+1)}}$, $\tilde{\boldsymbol{\sigma}}_{(i+1)}$

5. CASE STUDY

5.1 Introduction of field test

The field test reported by Konrad & Ayad, 1997 is implemented to validate MFT. The test site is located in Saint-Alban, 80 km west of Québec City in the Saint Lawrence Valley. The Saint-Alban clay is a part of the Champlain Sea Clay deposits. The typical soil profile consists of 0.4 m of top soil, 1.2 m of weathered clay crust and the rest is the Saint-Alban clay which called intact clay in the case. A longitudinal cross section of the excavations is shown in Fig. 16. The study mainly concentrates on the upper intact clay layer, which had never been experienced to any freeze-thaw or wetting-drying cycles. Fig 17. Illustrates soil properties of upper 12 m. The deposit has not been subjected to any preconsolidation. According to properties shown in Fig 17., the intact clay deposit was in overconsolidate condition because current stress applied on soil is smaller than its history stress (Konrad & Ayad, 1997). Even though the soil is very sensitive clay, the sensitive behavior only appears when you at normal consolidation state. This means the deposit shows elastic property based on elastic-plasticity theory. Thus, elasticity is mainly used in model to simulate soil behavior in this research. Since no external stress applied to the field test, change of mean stress in soil unit is small.

The first cracks occur after about 17 hours from the beginning of evaporation. This was the first observation made during the following field test and does not necessarily correspond to the actual time of crack initiation. After 27 h of evaporation, the average gap between cracks was about 5 mm while it changes to 4 mm after 48 h of evaporation, which indicating the soil volume shrinkage. After 96 h of evaporation, most of the soil polygon showed new cracks and the opening of cracks was about 5 mm. After 192 h, differential shrinkage, which leads to subhorizontal shear

planes, became noticeable in the upper 5 to 7 cm. Fig 18 presents the cracks formation after 182 h of evaporation. At that time, the opening of secondary cracks below the desiccated crust was only about 2 mm and reaching to 4.5 mm after 249 h of evaporation. Primary cracks at the surface were observed at about 17 h and secondary cracks formed at around 70 h. It appears that after the formation of secondary cracks, the rate of crack opening increased a little, which is possibly due to three-dimensional effect on moisture loss. The secondary cracks were initiated after about 150 h of evaporation according to extrapolation of observed data. Cracks and settlement occurred in the field test are mainly because of soil shrink based on moisture content change. This makes measurements of hydraulic properties significantly important.

5.2 Measurements of hydraulic properties

In Konrad paper, several important soil properties are measured during the experiment in separate time step which are 0 hours, 18 hours, 24 hours, 42 hours, 65 hours, 73 hours, 97 hours, 145 hours, 193 hours and 241 hours. The volumetric moisture content is measured by the TDR technique from which the gravimetric water content profiles inferred. Seven thermistors were installed at depths of 2, 4, 10, 20, 32, 46 and 69 cm. The validation of TDR is presented in detail in Konrad paper. High quality 200 mm diameter samples are retrieved to measure volumetric moisture content for the validation. The agreement is excellent, indicating the TDR is suitable to measure moisture content in the field test. Water content profile is shown in Fig. 19. After 18 h of evaporation, the water content at 2 cm below the ground surface decreased from 103 to 94 % while that below around 30 cm remained unchanged. With evaporation going, the moisture content keeps decreasing especially in the upper 40 cm. After a close examination of water profile in Fig 19, a change in the shape of water content profile can be noticed taken at 73 h evaporation. It suggests

an increased water content loss and maybe a transition from one-dimensional to three-dimensional evaporation.

The soil-water characteristics curve of Saint-Alban clay retrieved from a depth of 2 m is provided in Fig 20. Suction profile is measured by tensiometer, but some errors were observed after suction reaches approximately 30 kPa. It happened probably because of the presence of air in the tubes. Thus, the extrapolated suction is inferred based on the soil water retention curve shown in Fig 20.

Evaporation flux has important influence on the propagation of cracks. However, no direct measurements are available till now. The rate of moisture loss per unit area is calculated based on the porosity profiles shown in Fig 21. Porosity of the clay in field test was changing along with different time step and depth. After crack formation at the soil surface, moisture loss is associated with three-dimensional instead of solely to one-dimensional evaporation. Thus, the rate of moisture loss is expected to increase with time after crack formation but also decrease subsequently because of a reduction in hydraulic conductivity in upper soil layer based on the water content decreases.

5.3 Measurements of mechanical properties

Vertical settlement and horizontal shrinkage are results of soil volume change induced by capillary based on evaporation. Vertical settlement is measured by eight settlement gauges placed at the periphery of the excavation. Fig 22 illustrates the evolution of vertical settlement at depths of 2, 4, 7, 10, 16, 25 and 40 cm. A maximum settlement of 4 mm was observed at the surface of the soil, while soil at 40 cm depth never displayed any settlement during the whole test period. Vertical settlements were only observed in the first 5 to 7 cm of the clay deposit while the water

content remains to change across the first 30 cm. This is because when the vertical cracks developed into around 5 to 7 cm, further moisture change induced essentially a volume change in the lateral direction associated with crack opening. After lateral cracks appear, three vertical cracks formed within each polygon and propagated to a depth of about 4 to 6 cm, which corresponds to the length of the stem of the observed protuberances in each polygon. In the central part of a polygon, the vertical cracks form along a cylindrical surface. Continued moisture loss in each polygon leads to crack opening as shrinkage increases. Fig 23 shows the volume decrease of the stem creates a spherical cap in its lower part. Fig 24 illustrates protuberances figured out in test field.

5.4 Crack propagation mechanisms during desiccation

Reason of cracks propagation is because of stress concentration in the vicinity of the crack tip. The depth of cracks is controlled by both the intrinsic soil properties and the stress field. Three modes are introduced for cracks propagation before. Mode I explains propagation of cracks because of opening of material. Model II or an in-plane fracture mode regards cracks propagation based on shear strength and mode III takes torsion into consideration for cracks initiation. In this field test, primary cracks, which formed short of 17 h of evaporation, propagation is explained with Model I. The probable depth of primary cracks is around 5 cm according to settlement profile. Secondary cracks didn't begin to propagate until 70 and 80 h. With process of evaporation, subhorizontal shear planes appear at depth of 5 and 7 cm.

Three-dimensional effects of soil lead to shear plane due to differential shrinkage. The shear plane, which can be explained refers to mode II fracture mechanism, is horizontal in this case and the cracks propagate horizontally as well. The length of the crack propagation is

controlled by the magnitude of shear stress. According to the observed data, the vertical secondary cracks propagated below the shear plane after about 150 h of evaporation. Two mechanisms are introduced in Konrad et al. (1997) paper to explain sudden crack propagation below the horizontal shear plane.

The first method is regarding the existing cracks subjected to increasing total horizontal tensile stresses propagate suddenly to the ultimate depth when the stress intensity factor reaches the critical value K_{Ic}. However, the K_{Ic} is related to the moisture content of the soil and increase as moisture content decrease. This explains the tensile stresses required for cracks formation in this stage is higher than that required for original crack initiation.

The second option is to assume the mechanism of crack propagation below the subhorizontal shear plane is the horizontal total stress reaches the tensile strength of the soil to crack soil, as illustrated in Fig 19. The second stage of the crack propagation starts at around 150 h after evaporation. At that time, the water content is was lower than the original value of 103%. Therefore, the tensile strength is higher than that of the soil at its original water content.

To summary, there are six events to describe the suggested mechanisms during the first 250 h of evaporation. First, the initiation of primary cracks leading to a crack depth of 5 cm and a spacing between 20 and 24 cm before 17 h of evaporation. Secondly, cracks keep propagating due to moisture change. Thirdly, the initiation of secondary cracks after 70 h when tensile stress reaches the tensile strength of desiccating soil. Fourth, horizontal strains induced in a plane at a depth of about 6-8 cm. This leads to a subhorizontal crack. The fifth stage is about the initiation and propagation of new cracks below the horizontal crack. Finally, continued evaporation and volume change creates the observed protuberance in each polygon.

Based on test results from Konrad paper, a simulation model is established to match the results. Most important part is to match settlement result and get cracks formation. This is significantly important for validating the MFT.

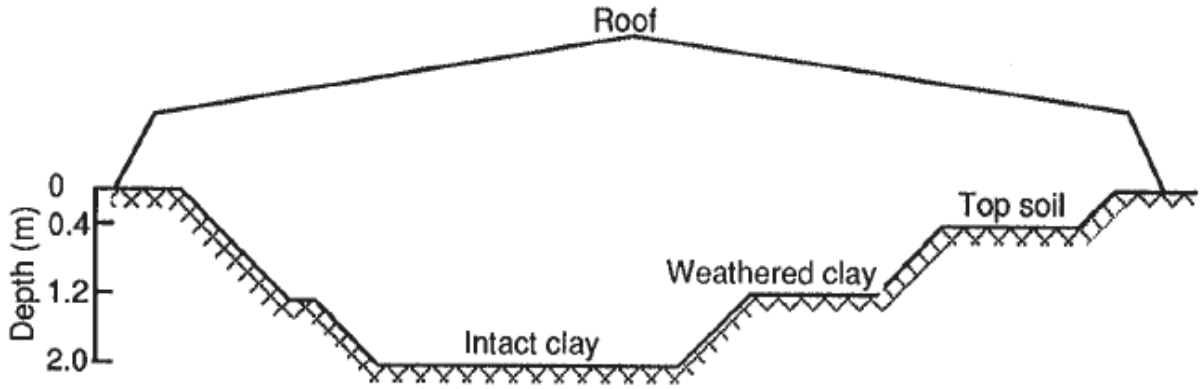

Figure 16 Characteristics of test sections (reprinted from Konrad & Ayad, 1997)

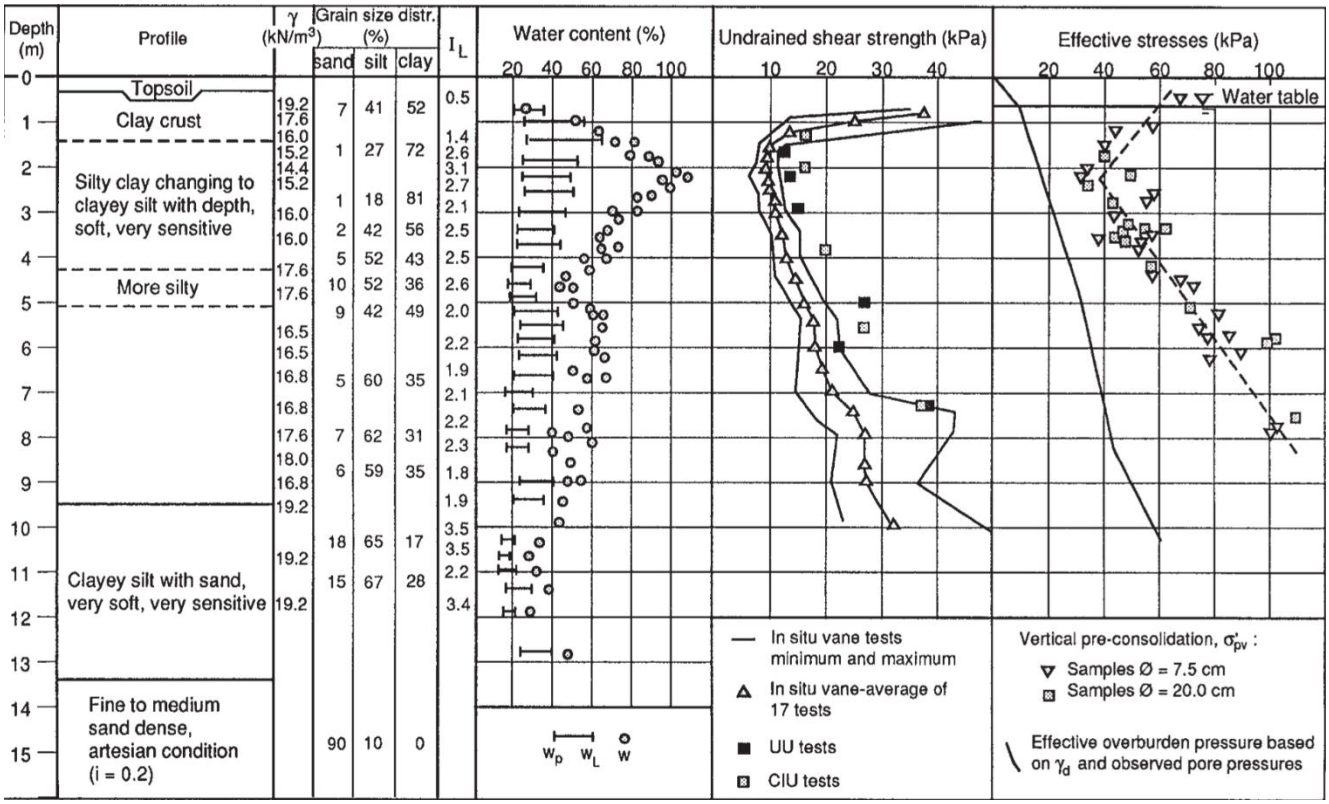

Figure 17. Soil profile at the field test (reprinted from Konrad & Ayad, 1997)

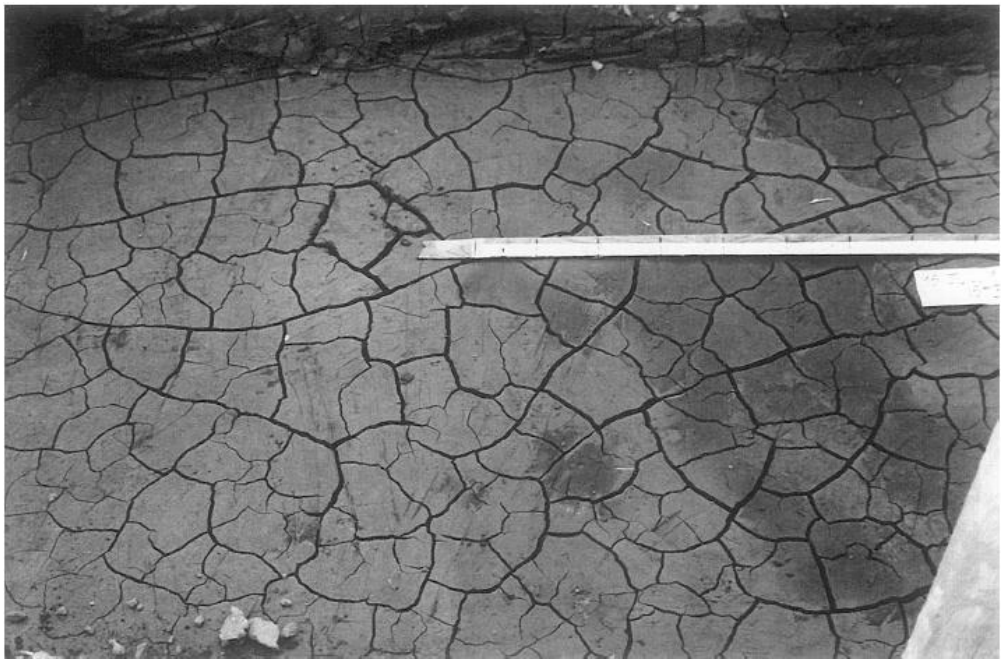

Figure 18. Crack network at the surface of clay after 182 h of evaporation (reprinted from Konrad & Ayad, 1997)

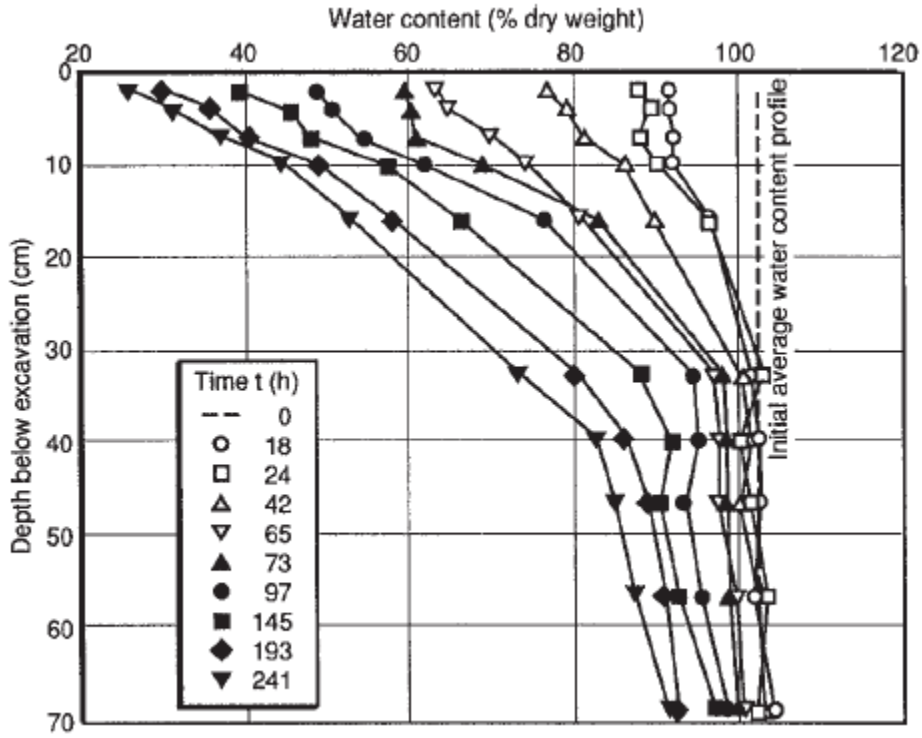

Figure 19. Water content profile at different elapsed time (reprinted from Konrad & Ayad, 1997)

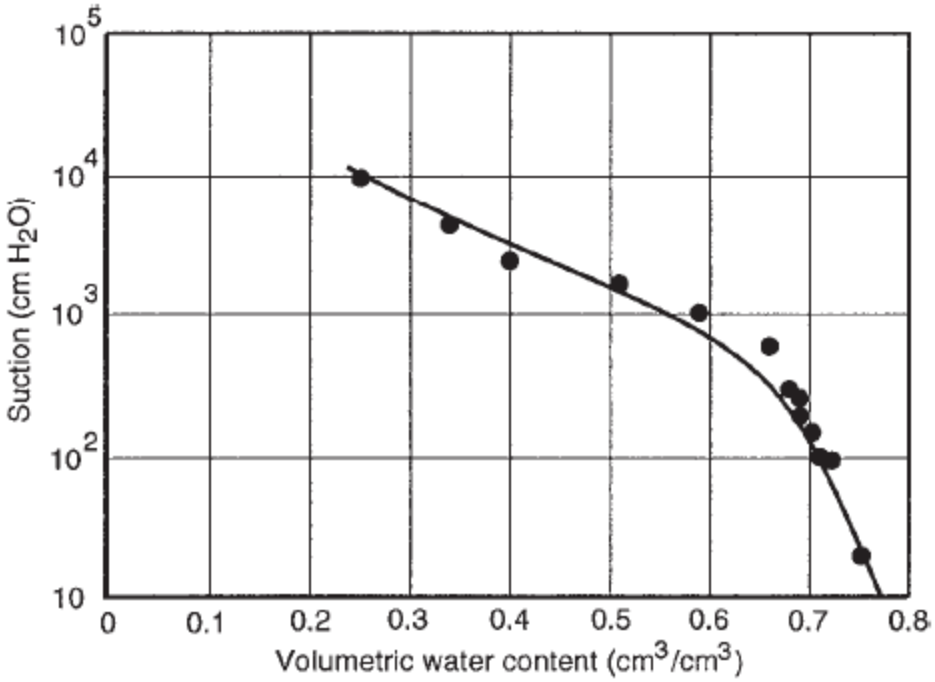

Figure 20. Soil-water retention curve for intact clay (reprinted from Konrad & Ayad, 1997)

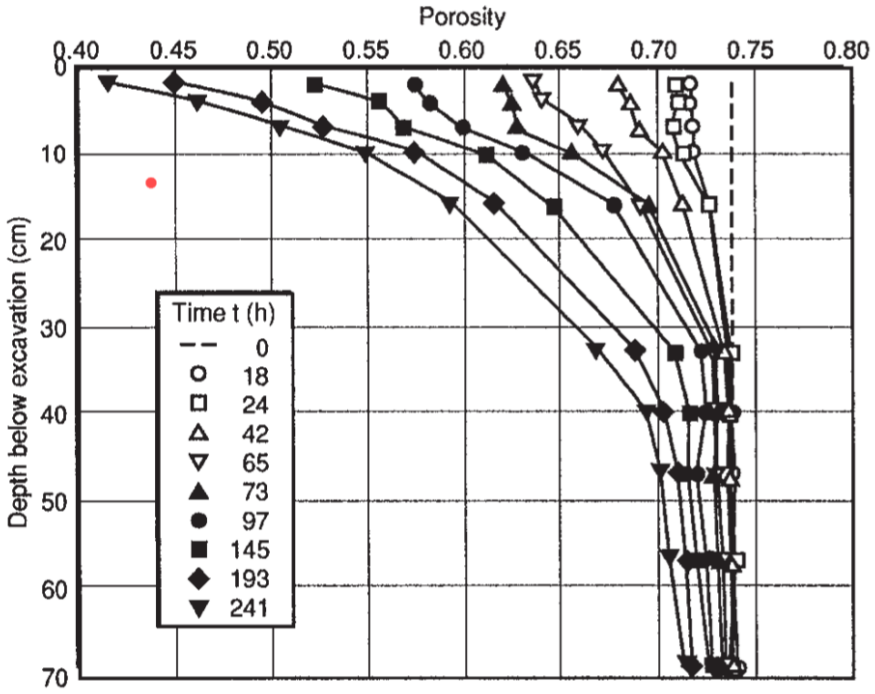

Figure 21. Porosity profiles at different elapsed times of evaporation (reprinted from Konrad & Ayad, 1997)

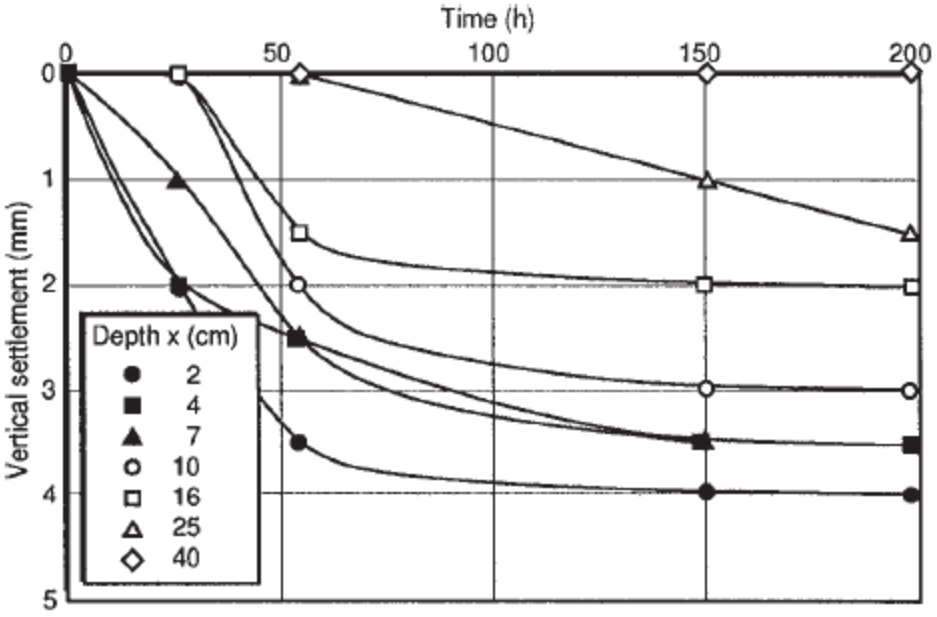

Figure 22. Settlement with time at different depths below the excavation floor in intact clay (reprinted from Konrad & Ayad, 1997)

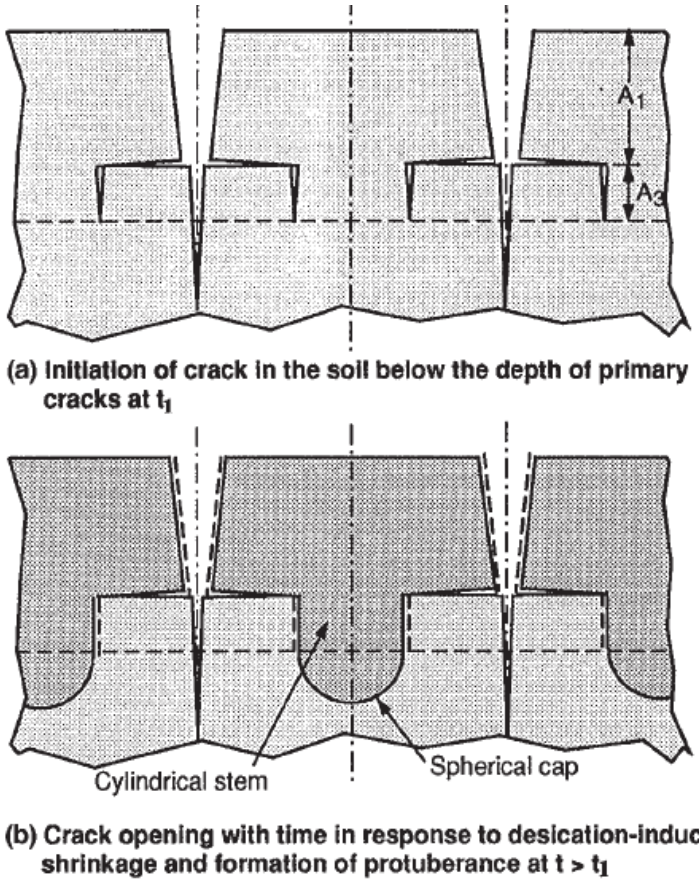

(a) Initiation of crack in the soil below the depth of primary cracks at t_1

(b) Crack opening with time in response to desication-induced shrinkage and formation of protuberance at $t > t_1$

Figure 23. Description of mechanisms leading to vertical cracks below shear plane and formation of a protuberance (reprinted from Konrad & Ayad, 1997)

Figure 24. Polygon removed from the desiccated intact clay after 2 h (reprinted from Konrad & Ayad, 1997)

6. NUMERICAL ANALYSIS

6.1 Introduction

This research is operated in the finite element program CODE_BRIGHT(Olivella, Gens, Carrera, & Alonso, 1996). This computer code is established to solve coupled Themo-Hydro-Mechanical (THM) problems in porous media. The main THM phenomena and their mutual interactions are expressed mathematically based on constitutive equations; momentum, mass and energy balance equations and equilibrium restrictions. The main phenomena considered are water flow, air flow, gas phase, air solution in water, dissolved air diffusion, energy transfer, elastoplastic mechanical behavior of soil. Equilibrium restrictions associated with the amount of dissolve air in water in terms of the partial pressure of the air while the amount of vapor water on gas phase depending on pressure and temperature. This formulation has been widely validated in geological media(A. Gens et al., 2009; Pereira, Guimarães, Horowitz, & Sánchez, 2014; M. Sánchez, Gens, & Guimarães, 2012).

CODE_BRIGHT was not developed originally to simulate the crack propagation in porous media. The model was established based on Mesh Fragmentation Technique (MFT). MFT is based on the usage of interface solid finite elements with a high aspect ratio (O. L. Manzoli et al., 2016) which are inserted in between standard (bulk) finite elements of a finite element mesh. The MFT was implemented in CODE_BRIGHT based on ideas published by Sanchez et al. (Marcelo Sánchez et al., 2014b). By using the technique, it is possible to include the formation and propagation of cracks in the numerical analysis. CODE_BRIGHT uses GID and gmsh to generate mesh and shown results from simulation. The behavior of the regular elements of the mesh is introduced with the Barcelona Basic Model (BBM). The tensile damage model is adopted to

reproduce the behavior of the interface element. In following sections, two different mesh is produced for different aim of simulation. Simple mesh is created for parametric studies which are helpful to understand how different parameters influence propagation of cracks and theses parameters can subsequently be used into excavation case. Excavation case is established for simulation formation of cracks in filed test. The mesh is in bigger scale than simple case and is important to validate MFT.

6.2 Parametric studies

Parametric studies are processed with mesh of simple case. A simple and fast case is created for parametric study which shown in Fig 25. Fig 26 presents the inter face element inserted between the bulk element. Scale of the mesh is present in Table 3. Table 4 presents mechanical parameters used in reference case. Fig 27 is formation of cracks in reference case. Other cracking results of cases are compared with reference case. Cracks depth in reference case varied from 29 cm to 68 cm while space between cracks varied from 32 cm to 100 cm.

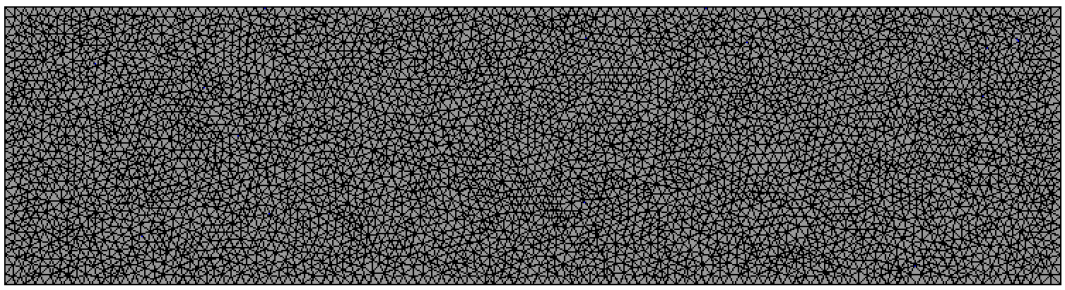

Figure 25. Mesh of simple case

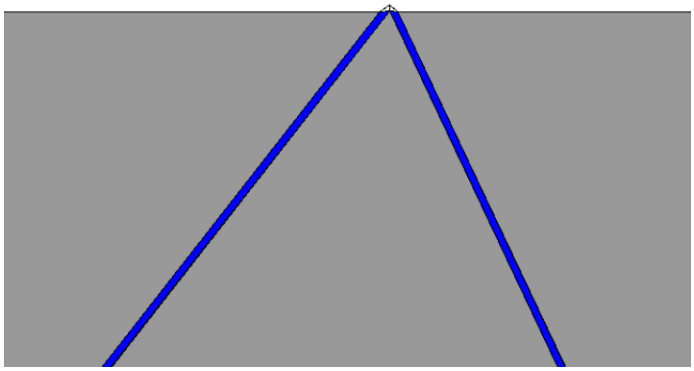

Figure 26. Interface element in simple case

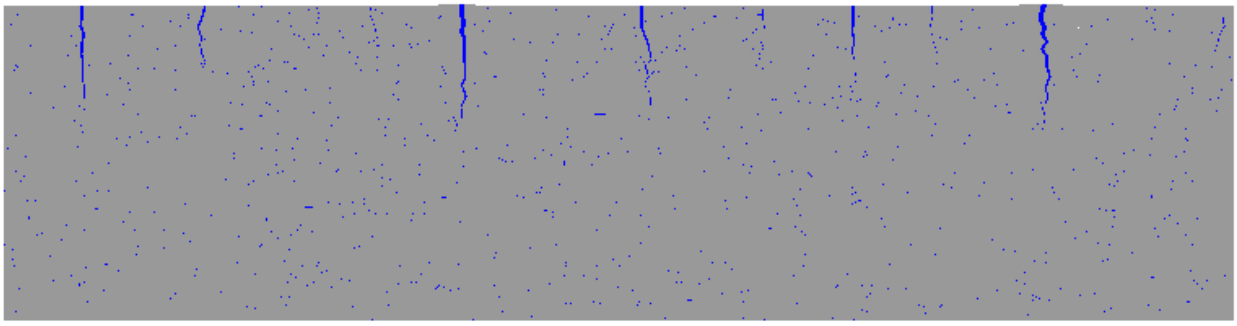

Figure 27. Formation of cracks in reference case

Table 3. Scale of the simple mesh

Scale of the simple mesh	
Length (m)	8
Depth (m)	2
Number of total nodes	29,071
Number of total elements	57,584
Number of interface elements	24,520

Table 4. Mechanical parameters for reference damage model

Mechanical parameters for reference damage model			
G_f (N/m)	q_0 (kPa)	k_{i0}	k_{s0}
25	10	0.01	0.005

After inputting different damage parameters into this model, cracks propagation influenced by different parameters can be observed. Fig 28. illustrates how fracture energy influence cracks propagation. As we can see, the less fracture energy it needs, the more fractures initiate. Fracture energy not only influences the depth of cracks but also the distance between cracks. It shows that less fracture energy is going to make more spread and deeper cracks. It totally makes sense because fracture energy is energy spent in fracture unit, which means it is easier to overcome small amount of fracture energy to get cracks. Fig 29 presents how tensile strength influence cracks propagation. Because tensile strength is the criterion to estimate whether soil would open, it would be hard for cracks to open if you have high tensile strength. Results in Fig 25 prove this hypothesis. The more tensile strength, the harder it is to open cracks. According to Fig 30, k_{i0} doesn't have much influence on the crack propagation. However, k_{s0} have a significant impact on formation of cracks. According to Fig 31, more k_{s0} leads to more cracks in soil. Reason is simple. For this model, no external stress except for gravity is loaded on the soil, which means cracks initiate because of suction. In this research, suction most influence mechanical properties of the model. k_{s0} is parameter in suction part of mechanical constitutive model so it is reasonable that k_{s0} has more influence on cracks than k_{i0}.

Since suction has more influence on cracks propagation in this case, the simple case is still used to study hydraulic and mechanical properties in model and comparing them with results captured in field test. Following part will introduce simulation in simple case in details

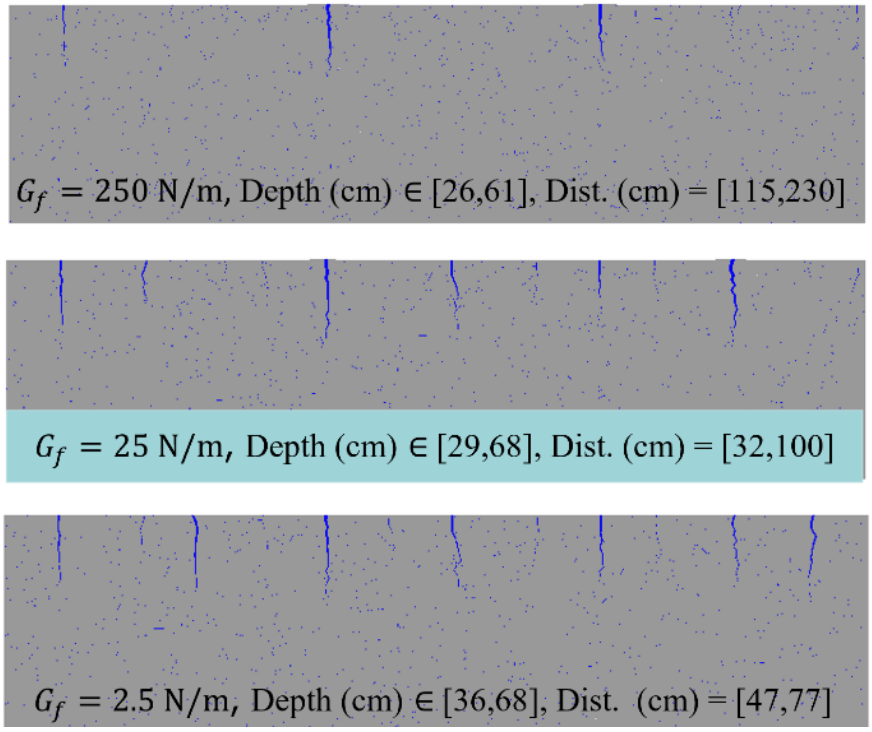

Figure 28. Cracks deformation according to fracture energy

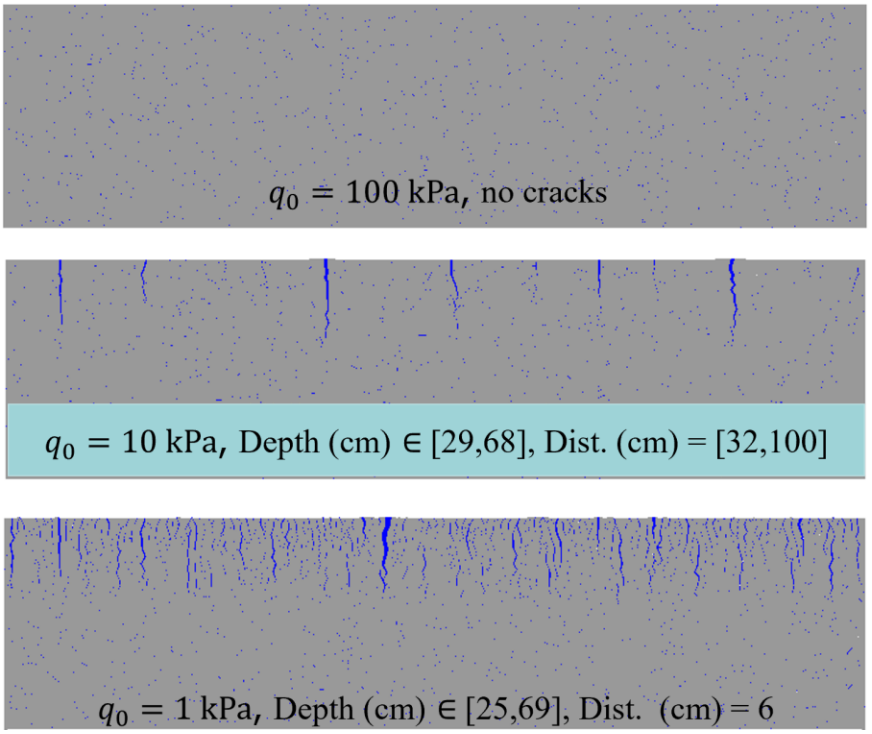

Figure 29. Cracks deformation according to tensile strength

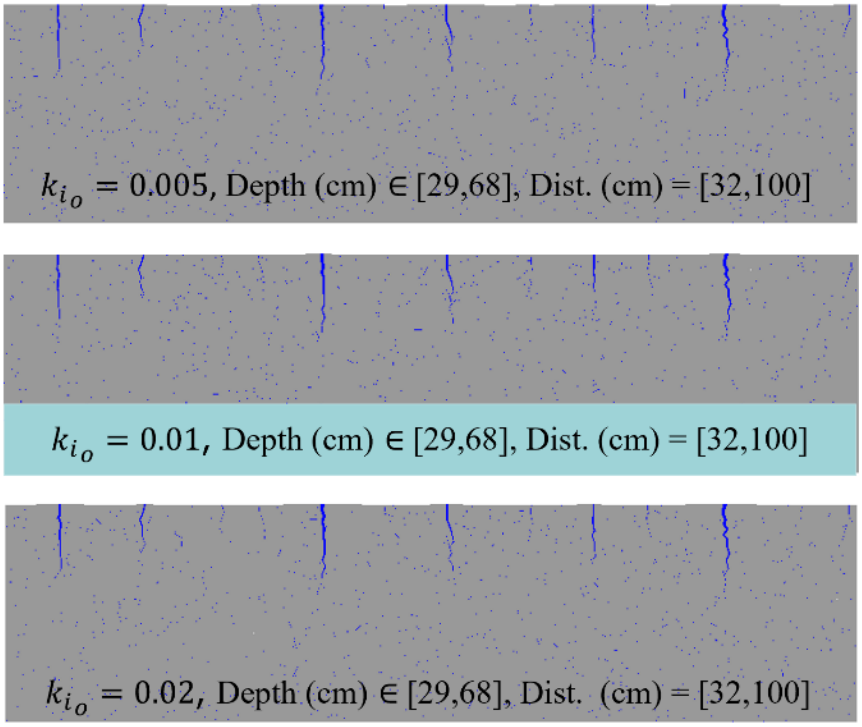

Figure 30. Cracks deformation according to k_{i0}

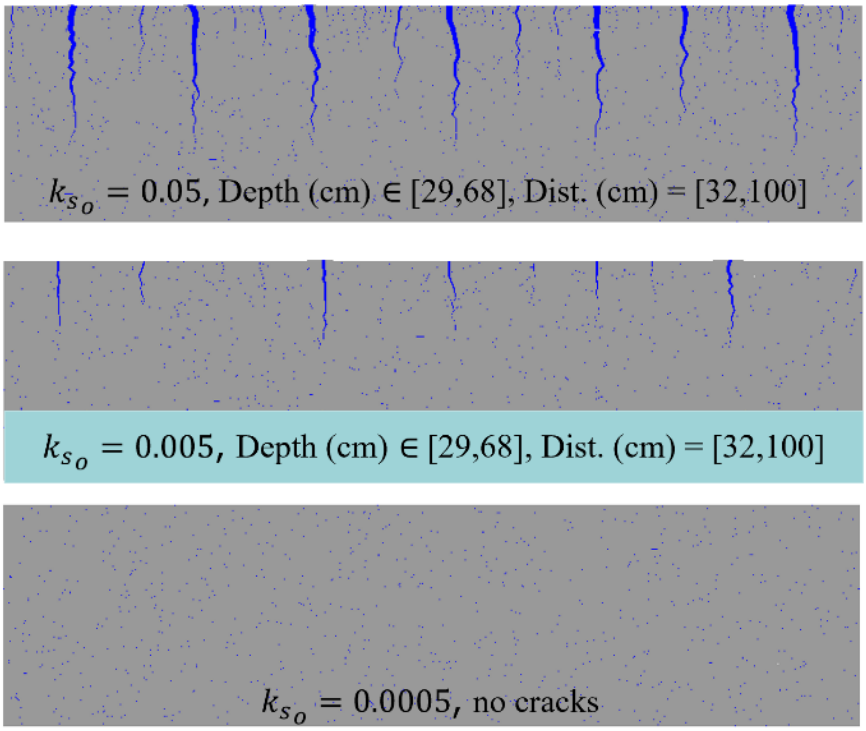

Figure 31. Cracks deformation according to k_{s0}

6.3 Simple case

6.3.1 Hydraulic properties of simple case

Hydraulic properties of the soil needed to match with that provided by Konrad (1997). Hydraulic properties are very important because it is directly related to water content of soil which significantly influences suction in soil. Suction have important impact on behavior of soil shrinkage because of capillary phenomena. As degree of saturation decrease, the radius of the meniscus decreases, which results in increase of surface tension based on capillary effect. The surface tension is named suction in geotechnical engineering. Suction provides source of tensile stress to drag soil material apart. When tensile strength exceeds tensile stress that soil can afford, cracks start to propagate in soil. In this case, soil-water retention curve is adopted to establish a relationship between suction and hydraulic properties (eg. water content, degree of saturation). Thus, the soil-water retention curve (SWRC) is checked first during this research. Fig. 32 shows result of SWRC match. The point line presents SWRC in field test while continuous line present analytical solution of SWRC used in model. Usually van Genuchten analytical solution is used to fix with field water retention curve, but in this case original van Genuchten analytical solution can't give a good fix result. So a modified analytical solution of the expression proposed by van Genuchten (1978) is adopted in this research (van Genuchten, 1978). The equation of modified analytical solution is:

$$S_1 = \left[1 + \left(\frac{s}{P_0}\right)^{1/(1-\lambda_0)}\right]^{-\lambda_0} f_d$$

$$f_d = \left(1 - \frac{s}{P_d}\right)^{\lambda_d} \tag{6.1}$$

where S_1 is degree of saturation, s means suction, P_0 means atmospheric pressure and λ are different model parameters. By choosing reasonable parameters in the analytical solution of SWRC, the relatively perfect match result is shown in Fig. 32. Table 5 shows parameter values in SWRC analytical solution.

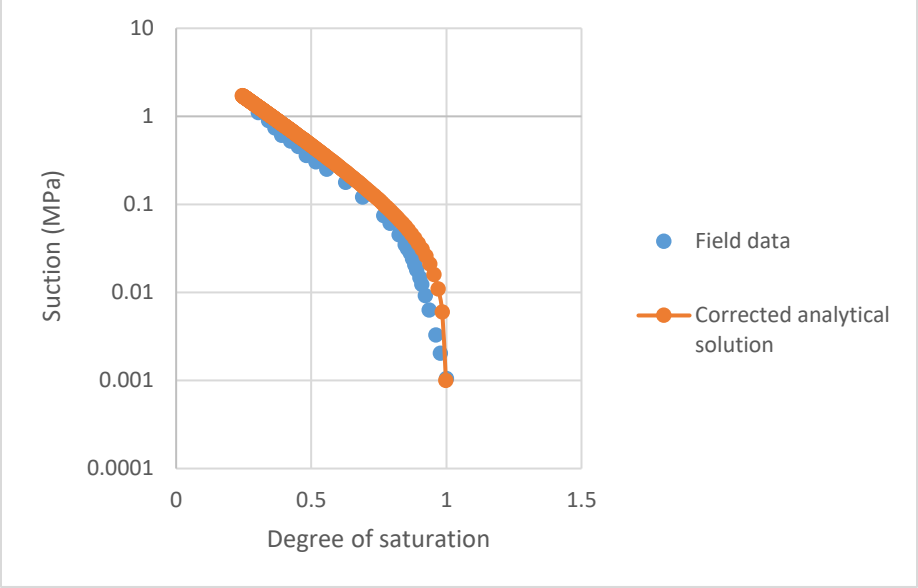

Figure 32. SWRC match result

Table 5. Parameters value in retention curve

Retention Curve	
P_0 (MPa)	0.05
λ_0	0.19
P_d (Mpa)	1200
λ_d	400

After comparation of SWRC, hydraulic properties are checked with that in Konrad Paper. Most of hydraulic properties are published by Konrad et al (1993). They make some tests of soil

in same field to get void ratio and hydraulic permeability (Konrad & Seto, 1993). It is important because hydraulic permeability influence how water content varies with depth. This can cause different influence on suction profile with the soil.

To get a reasonable permeability result, permeability equation is checked in the research. There is two common permeability in Geotechnical engineering. One is Kozeny's based model equation which is shown below:

$$\kappa = \kappa_0 \frac{n^3}{(1-n)^2} \frac{(1-n_0)^2}{{n_0}^3} \tag{6.2}$$

where κ is permeability, n_0 is reference porosity, κ_0 is permeability associated with n_0 and n is porosity.

Another equation is modified based on Kozeny model,

$$\kappa = \kappa_0 exp[b(n-n_0)] \tag{6.3}$$

where b is modified parameter to make equation more flexible to fix with field data.

In this research, reference porosity is chosen by calculating average value of porosity data shown in Konrad paper (Konrad & Seto, 1993). Matching result is shown in Fig 33.

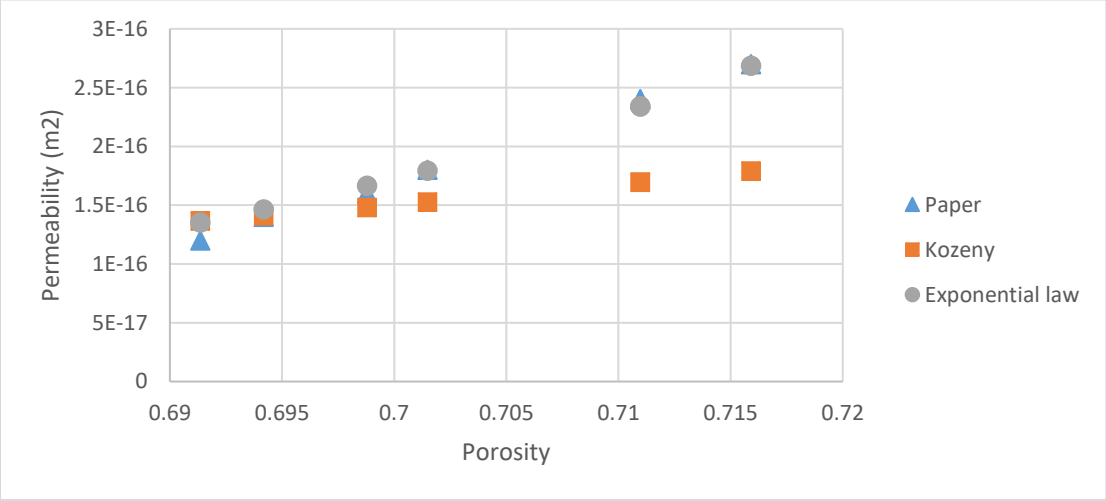

Figure 33. Hydraulic conductivity match results

In Fig 33, triangular points present data in field. Square points illustrate data from Kozeny basic model equation while circle points show data from modified equation. Parameters used in these two equations are shown in Table 6. Based on results shown in Fig 9, modified equation best fit with data in field test. Thus, parameters in modified equation are adopted and input to model in this research.

Table 6. Permeability value in model equation

Kozeny basic model equation	
n_0	0.7
κ_0 (m^2)	1.5E-16
Exponential equation	
n_0	0.69
κ_0 (m^2)	1.3E-16
b	28

Since water content is measured in field test, hydraulic properties in model can be verified based on matching results of water content. Fig. 34 illustrates matching results of the gravimetric water content depends on depth of different elapsed time between results from model and that from field test of Konrad in which circle point line presents data from model and square line means data from field test. From Fig 34, water content decreases with procedure of evaporation. Model provides good results in water content at different elapsed time and different depth. It proves the hydraulic properties of this model is good to go. Next step is to check mechanical properties.

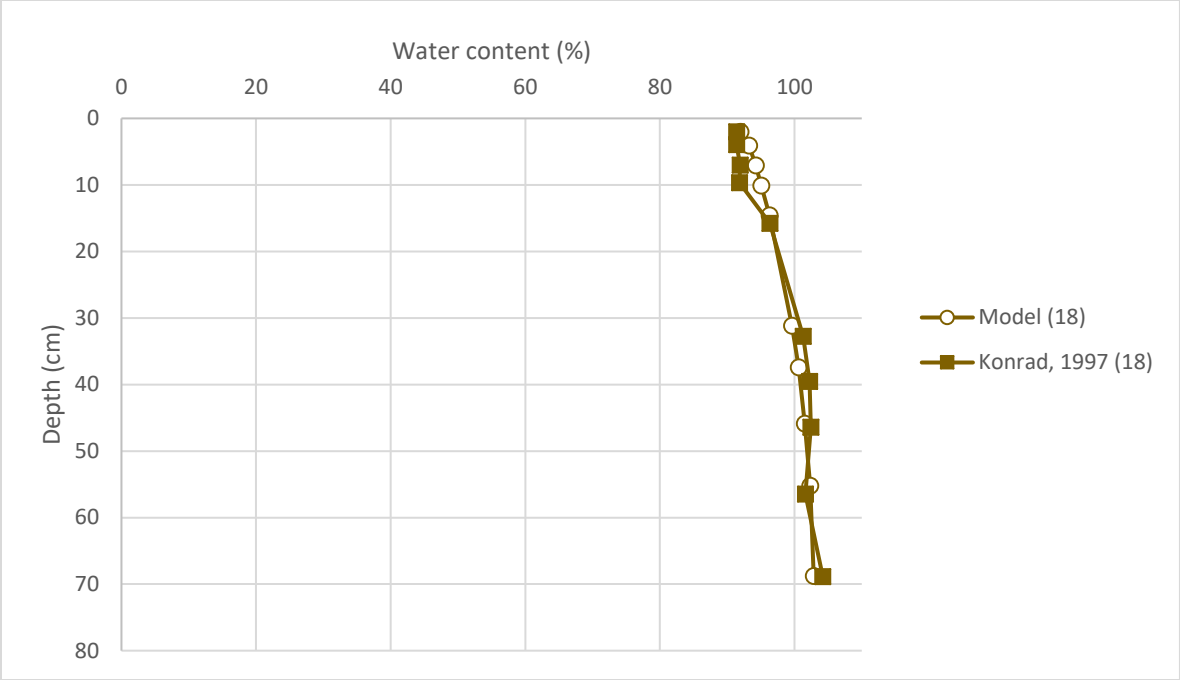

(a)18 hours after evaporation

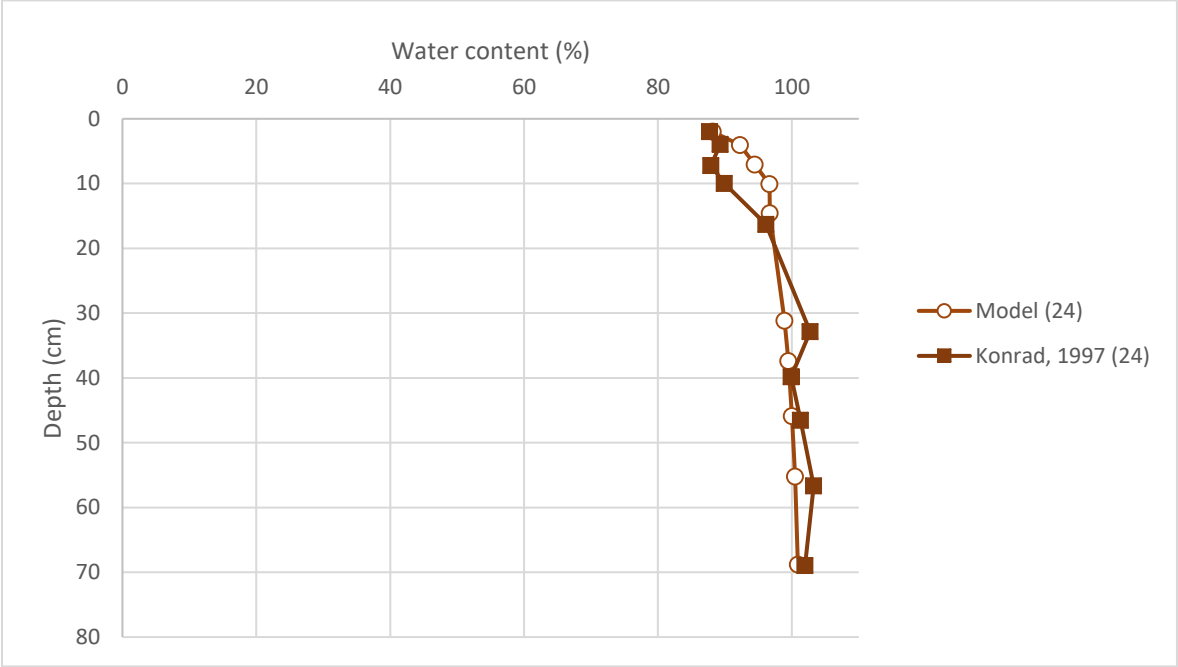

(b) 24 hours after evaporation

Figure 34. Matching results of the gravimetric water content depends on depth between simple case and field test

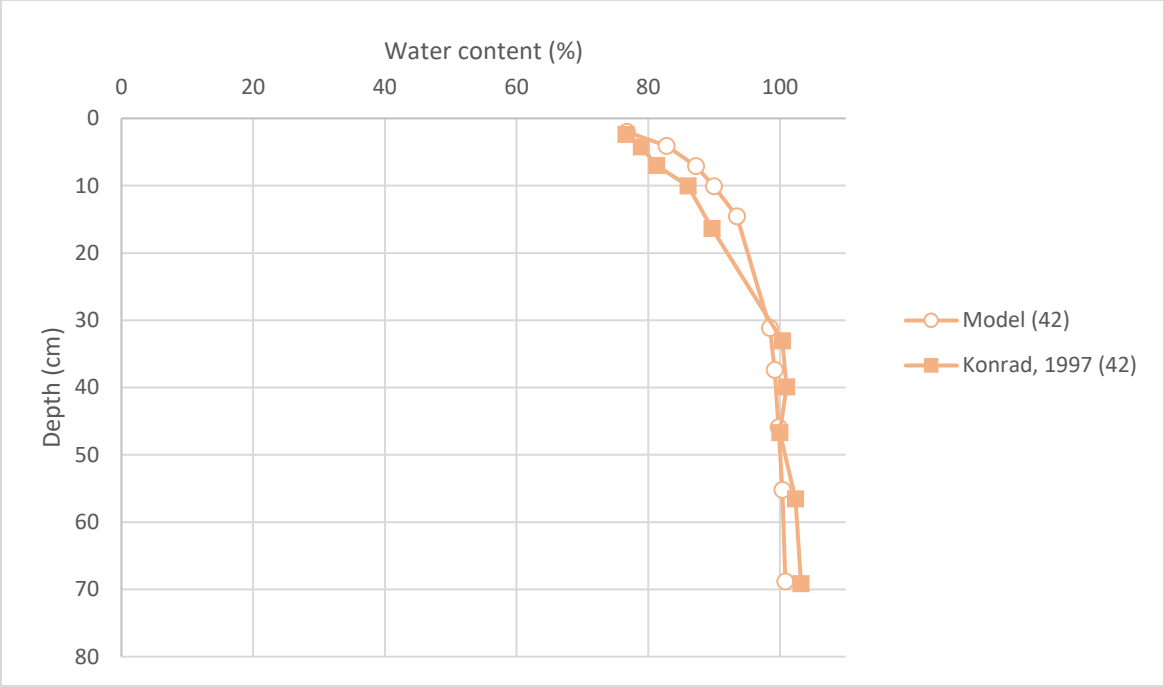

(c) 42 hours after evaporation

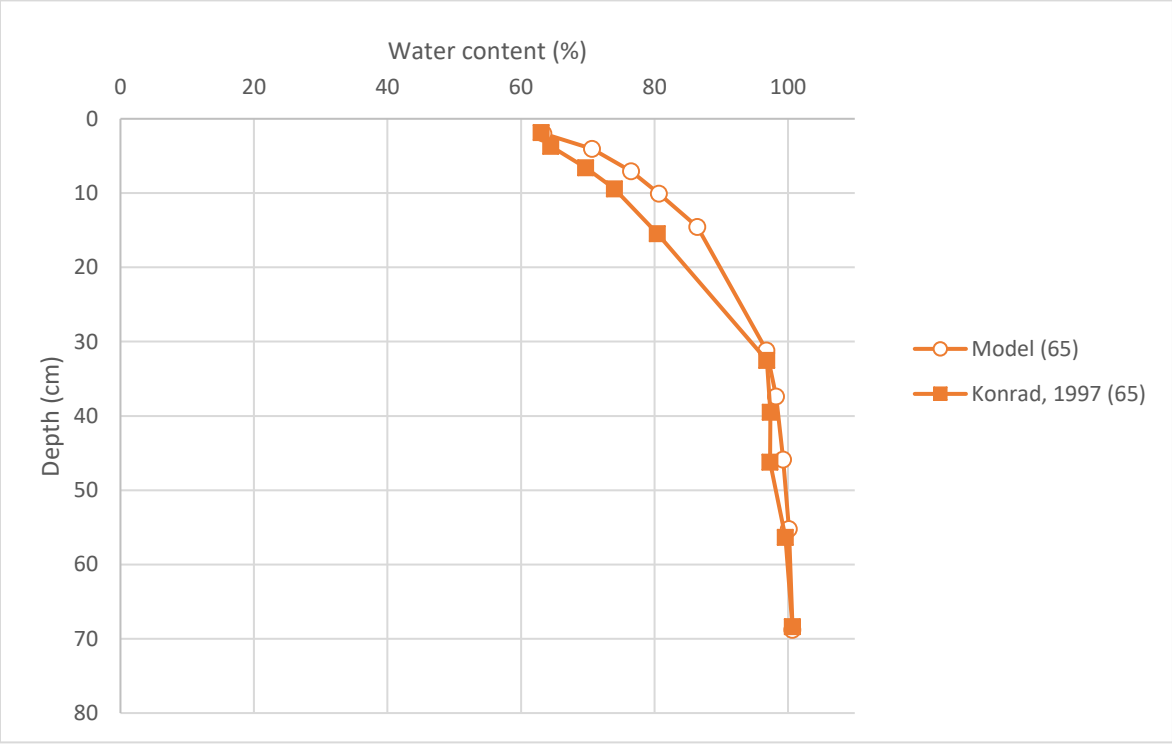

(d) 65 hours after evaporation

Figure 34 continued

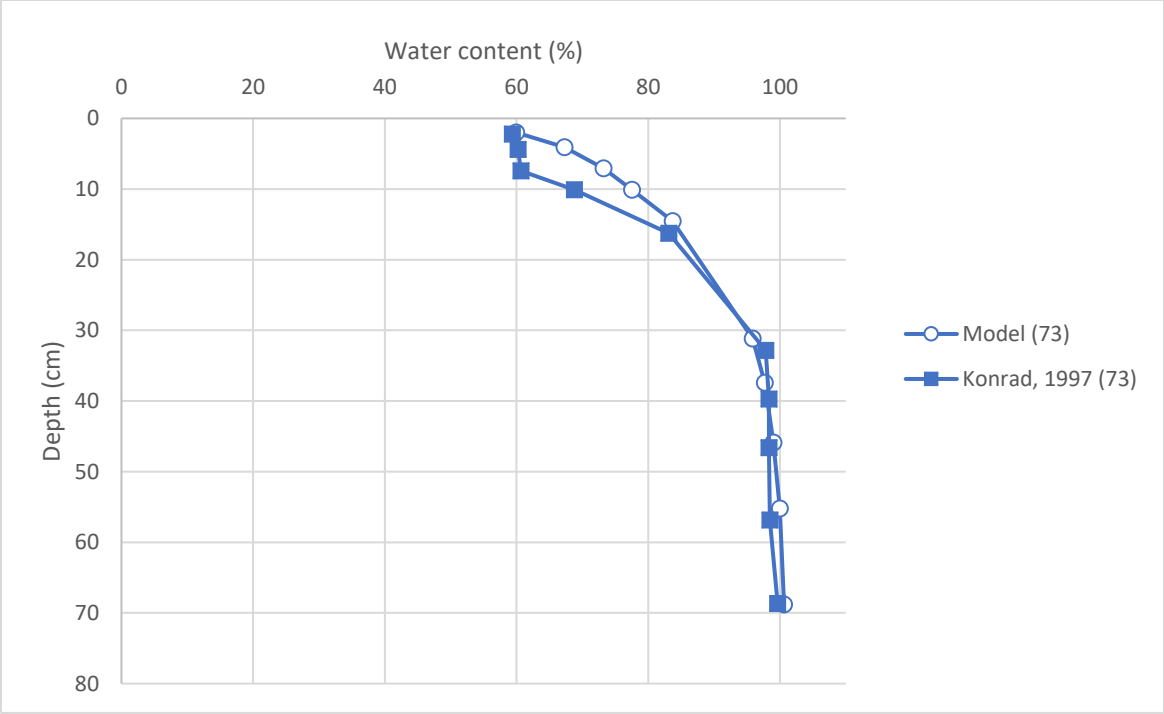

(e) 73 hours after evaporation

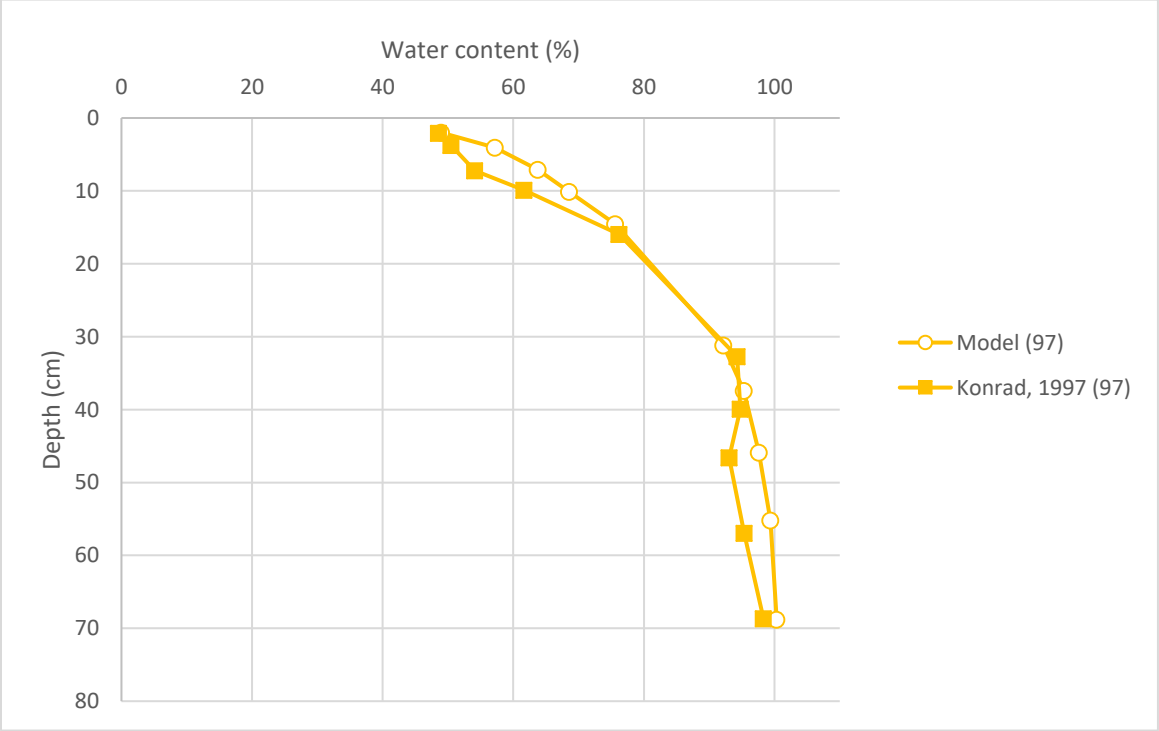

(f) 97 hours after evaporation

Figure 34 continued

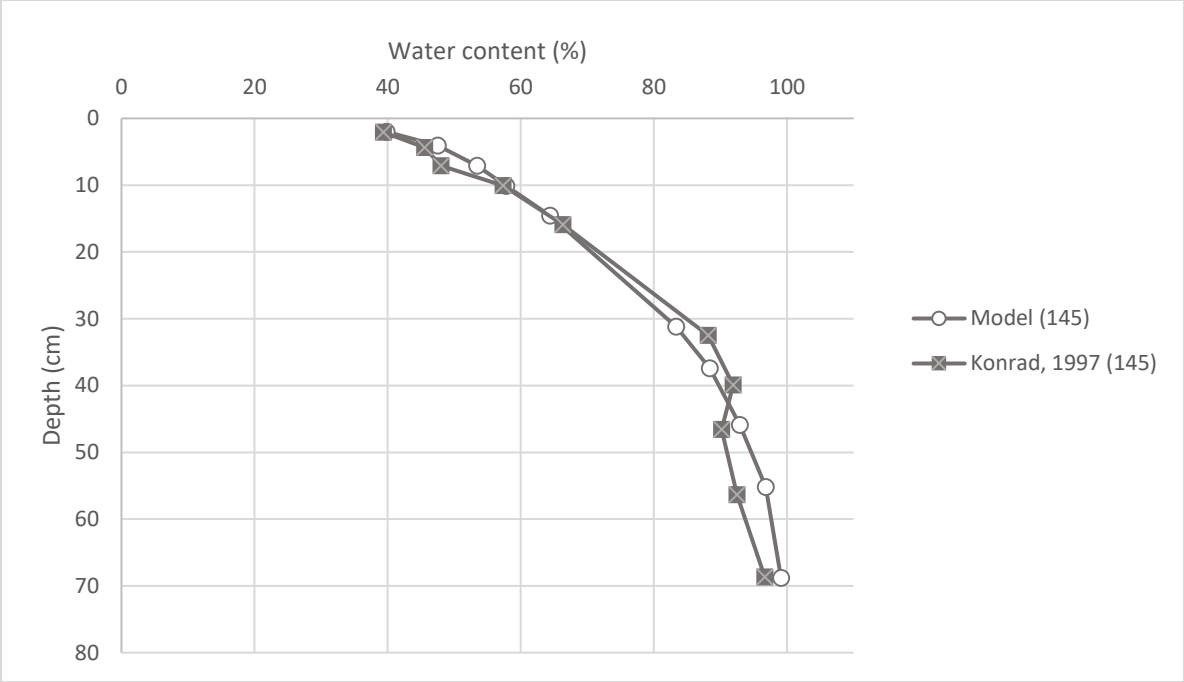

(g) 145 hours after evaporation

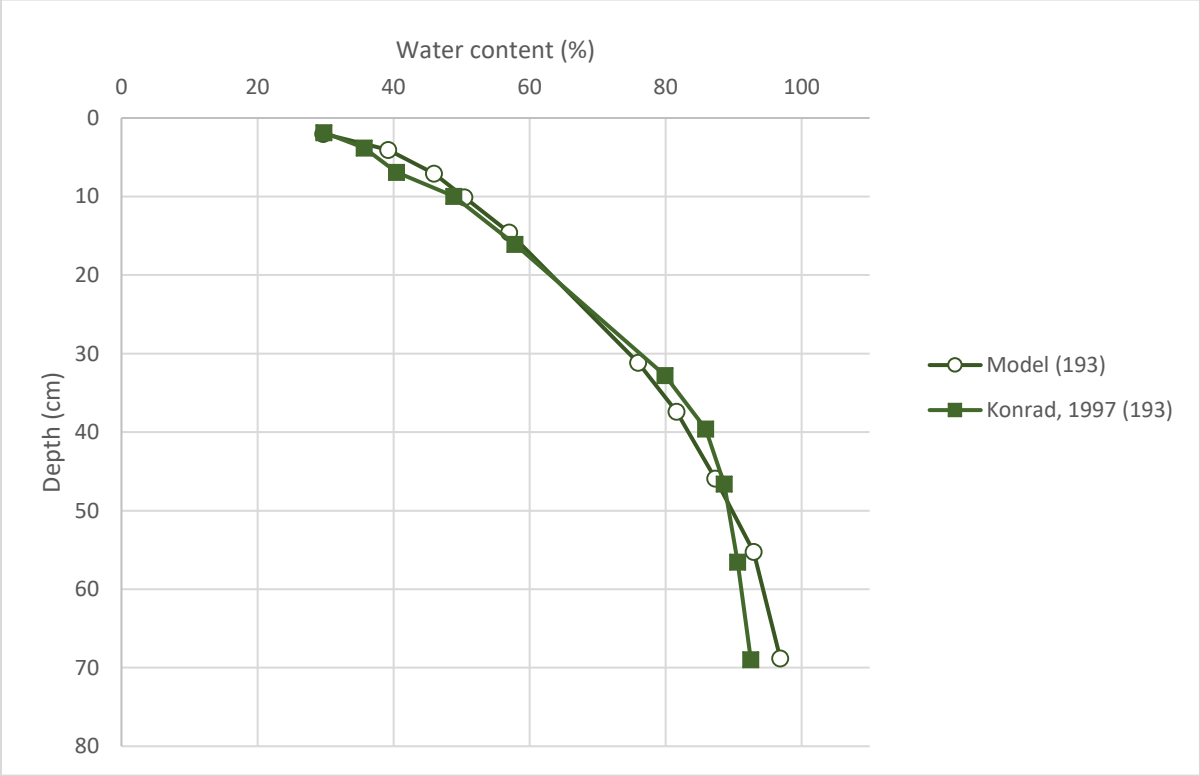

(h) 193 hours after evaporation

Figure 34 continued

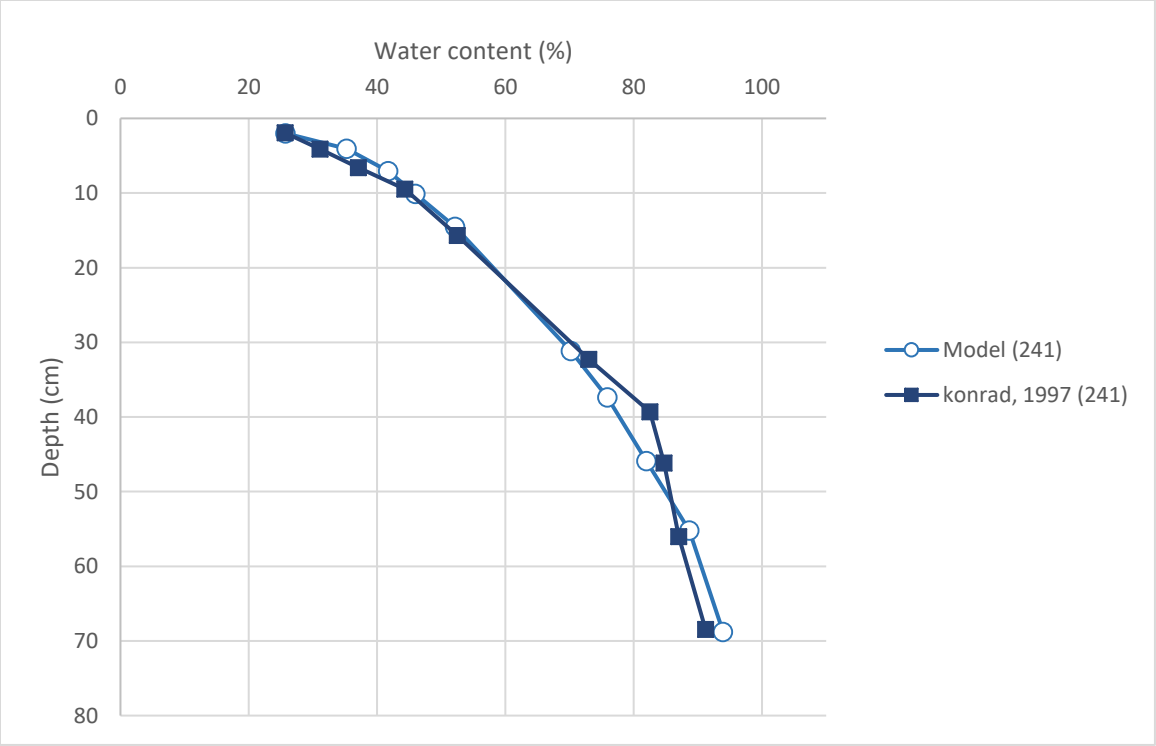

(i) 241 hours after evaporation

Figure 34 continued

6.3.2 Mechanical properties of simple case

For this simulation, the most valuable result is the settlement. The Barcelona Basic Model (BBM) is adopted to describe the behavior of the bulk elements of the mesh in order to estimate the amount of settlement. The following equation is to calculate settlement based on BBM:

$$d\varepsilon_v^e = \frac{k_i(s)}{1+e}\frac{dp'}{p'} + \frac{k_s(p',s)}{1+e}\frac{ds}{s+0.1} + (\alpha_0 + 2\alpha_2\Delta T)dT$$

where

$$k_i(s) = k_{i0}\,(1+\alpha_i s)$$
$$k_s(p',s) = k_{s0}\exp(\alpha_{ss}s) \qquad (6.4)$$

where ε_v^e is volumetric elastic strain which is settlement in geotechnical engineering, s denotes suction, e is the void ratio in soil, T is temperature, p' is mean stress and p_{ref} refers to the

atmospheric pressure, and α goes to different scalar variables in different function. A parametric study will be conducted in order to find a reasonable value for α.

In order to get reasonable settlement, relation of different parameters in mechanical constitutive model is studied. From the mechanical constitutive model, three parts included to influence elastic strain. They are mean stress, suction and temperature. For now, temperature is not considered because suction is most influence settlement in this research. Thus, the equation can be simplified as following,

$$d\varepsilon_v^e = \frac{dp'}{K} + \frac{ds}{Ks}$$

where:

$$\mathrm{K} = \frac{p'(1+e)}{k_i(s)}$$

$$K_s = \frac{(s+0.1)}{k_s(p',s)}(1+e) \tag{6.5}$$

Since differential change of mean stress and suction are same at every time step, K and Ks is most influence differential elastic strain. From the equation, relation of elastic strain and parameters is clear. With Ks increasing, elastic strain decrease, which means the soil becomes loose and vice versa. K has same relation with elastic strain as Ks does. As suction has more influence on settlement in this research, parameters in Ks are studied mainly. Because we need stiffer soil as settlement goes, differential change of elastic strain is decreasing which means Ks should increase. Relation between Ks and suction is illustrated in Fig 35. Parameters value in this relation curve is shown in Table 7. Table 8 illustrates mechanical variables of interface element which is used to simulate crack propagation. Based on these parameters, settlement can be mimic. Fig 36 illustrates settlement results from model and field test at 2 cm depth. It gives a good matching result at the end part of settlement.

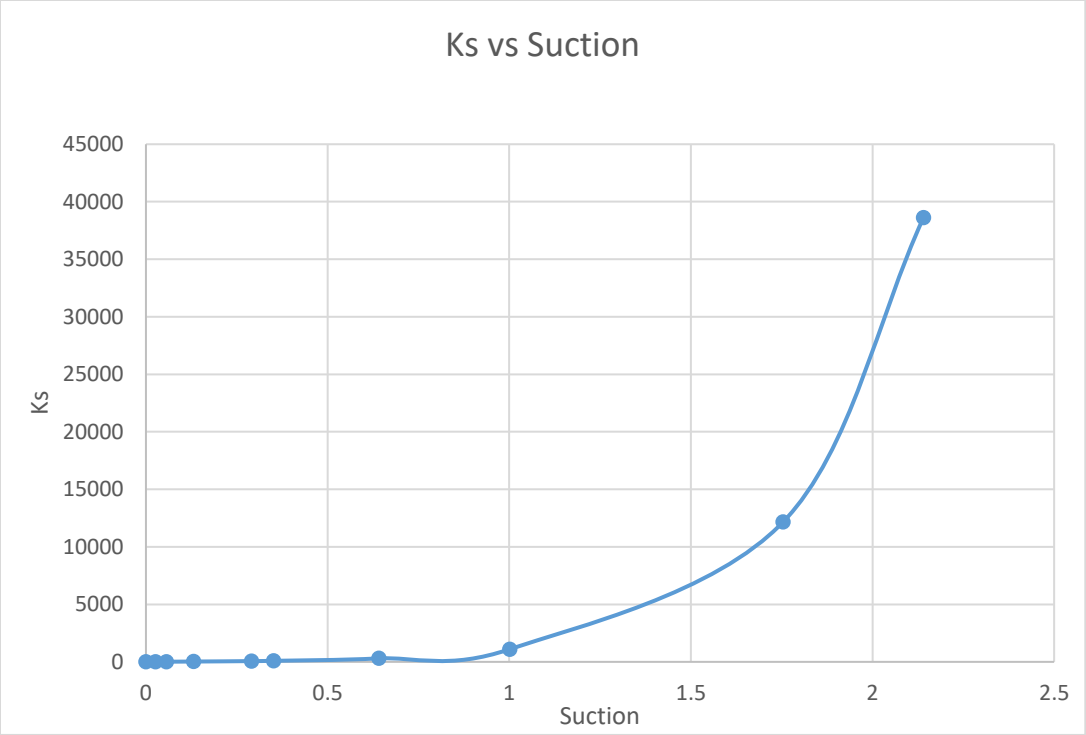

Figure 35. Relation of suction and Ks

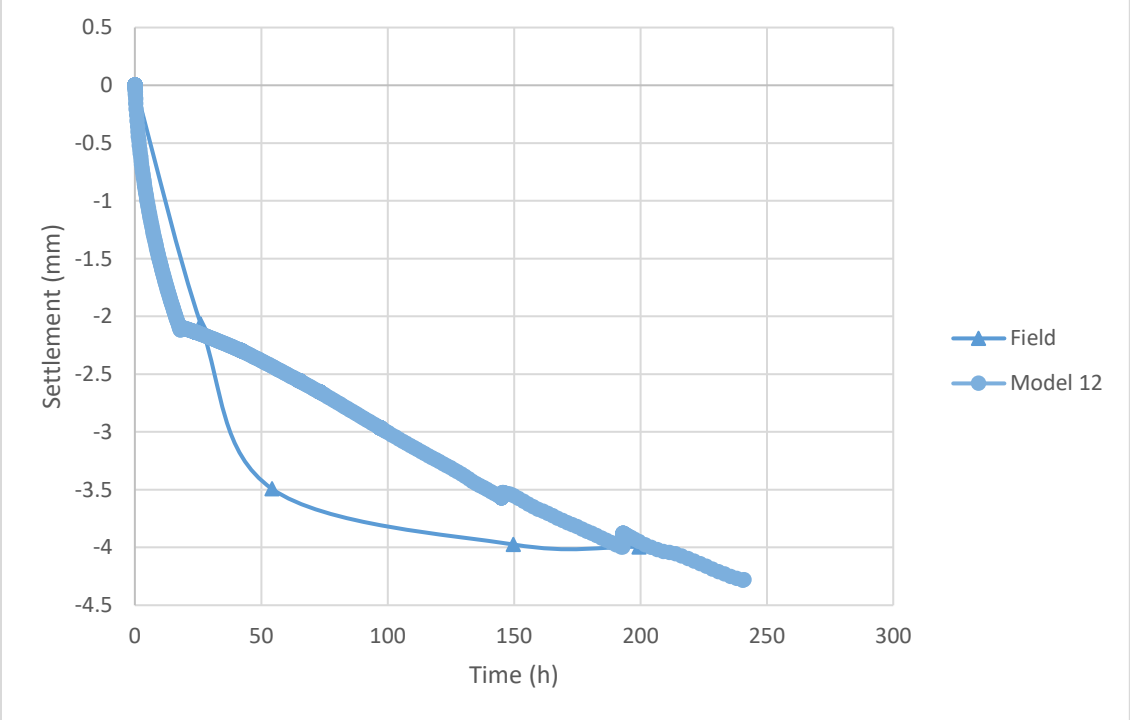

Figure 36. Settlement matching results at 2 cm depth with different elapsed time

Table 7. Mechanical properties of bulk element

Elastic parameters of BBM					
κ_{i0}	κ_{s0}	α_i	α_{ss}	p_{ref}	υ
0.05	0.025	0	-1.5	0.10	0.42

Table 8. Mechanical properties for interface element

Mechanical properties of interface element			
E (MPa)	υ	G_f (MN/m)	q_0 (MPa)
4	0	3.50E-7	0.01

Fig 37 presents cracks propagation and formation of the simple case. But the depth and space of cracks are different from field test. Cracks depth of model varied from 8 cm to 27 cm while that of filed test varied from 6 cm to 11 cm. Space between cracks in model in the range of 58 cm and 239 cm while that in field test is between 10 cm to 12 cm. Maybe the reason is the scale of the mesh. A larger scale mesh (excavation case) is introduced in following section to find out if scale of the mesh influences the propagation of cracks.

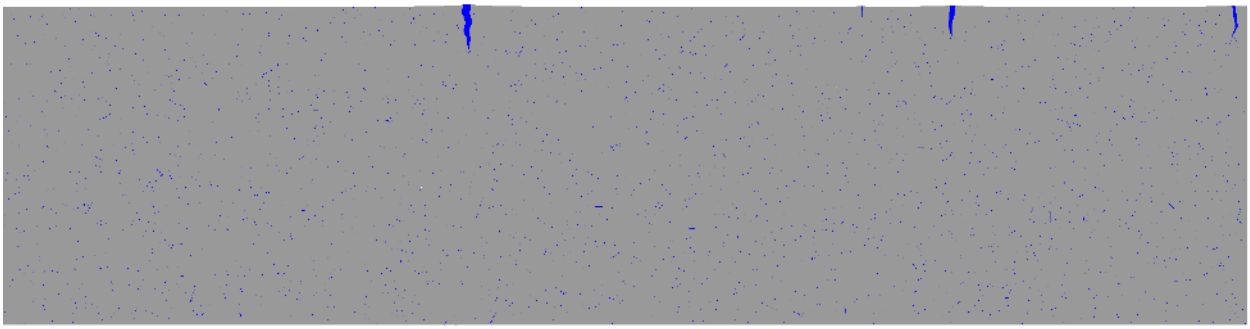

Figure 37. Example of drying cracks obtained with the MFT simulator

6.4 Excavation case

To simulate cracks propagation in field test, a mesh coupled with excavation process is created. Two procedures are created in this mesh to reproduce the field condition. One is the mesh before excavation starts, which is shown in Fig 38. Another is the mesh after excavation, which is illustrated in Fig 39. This process repeat the excavate procedure in field test. Interface elements are inserted into the mesh to capture formation of cracks (Fig.40). Because depth of cracks in the field varied from 6 cm to 11 cm, small scale mesh named ‘cracks section’ (dark brown part in Fig 39) with magnitude shown in Table is chosen at excavation surface to reproduce the propagation of cracks. Different parameters are used in different soil in the mesh. In this research, intact clay is mainly observed in field test. Thus, in the simulation, results in intact clay (cracks section and pink part below the cracks section) are captured to match with results in field test.

Figure 38. Mesh before excavation

Figure 39. Mesh after excavation

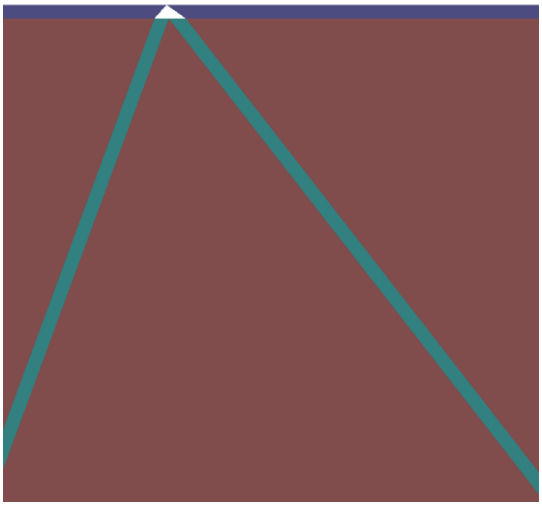

Figure 40. Interface element in excavation case

Table 9. Scale of the excavation mesh

Scale of the excavation mesh	
Length of intact clay (m)	20
Depth of intact clay (m)	7
Length of mesh of cracks section (m)	3.5
Depth of mesh of cracks section (m)	0.4
Number of total nodes	58,680
Number of total elements	118,014
Number of interface elements in cracks section	26,886

6.4.1 Hydraulic properties of excavation case

Since water content profile is matched in simple case, same water retention curve and permeability are used in excavation case to match water content profile. Fig 41. illustrates matching results of the gravimetric water content depends on depth of different elapsed time between results from excavation case and that from field test of Konrad in which circle point line presents data from model and square line means data from field test. It provides good results of gravimetric water content at different elapsed time. Then mechanical properties (e.g. settlement) are validated.

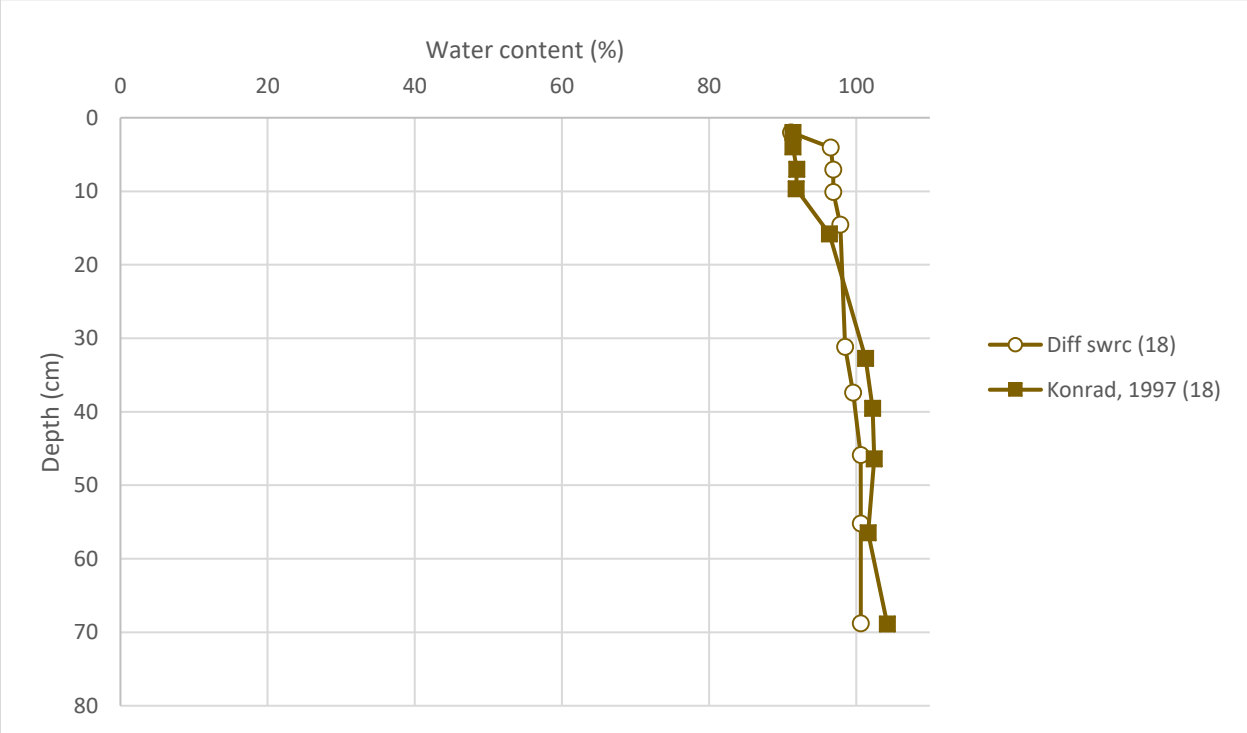

(a)18 hours after evaporation

Figure 41.Matching results of the gravimetric water content depends on depth between excavation case and field test

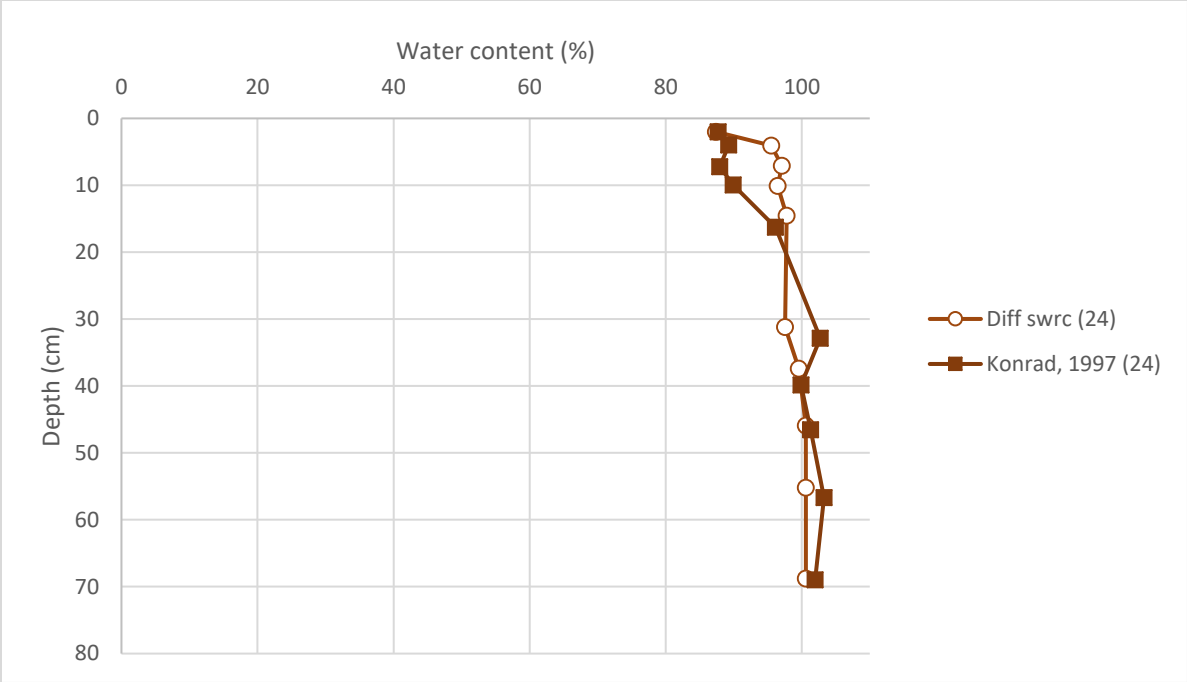

(b) 24 hours after evaporation

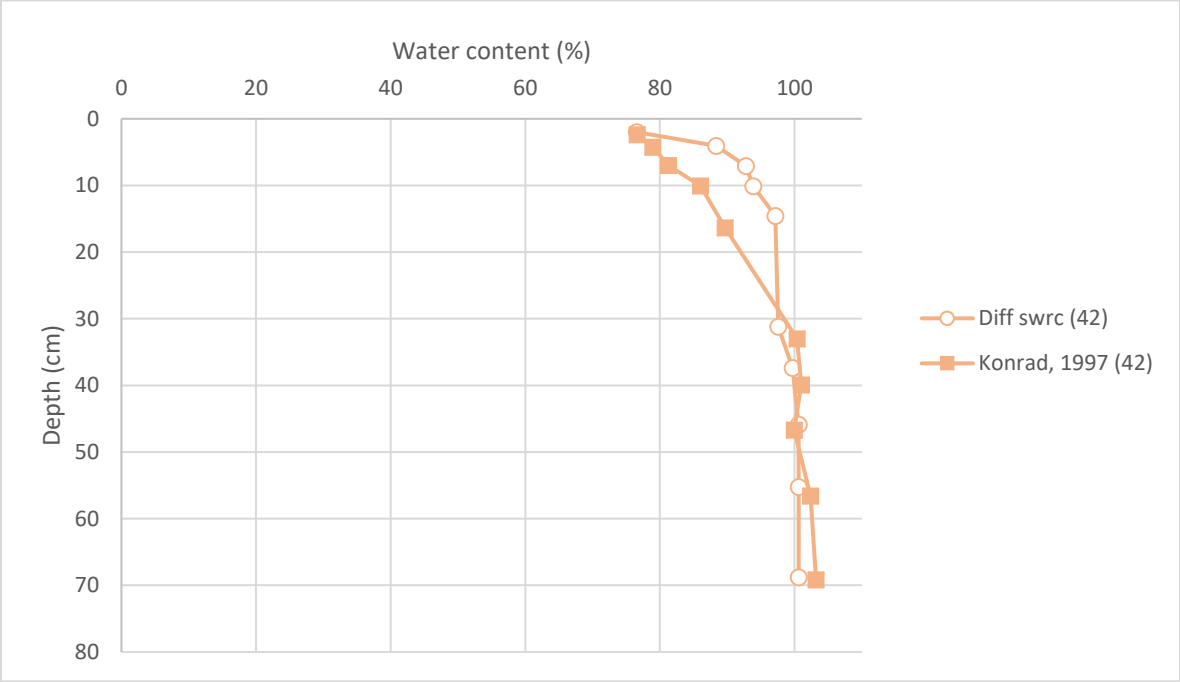

(c) 42 hours after evaporation

Figure 41 continued

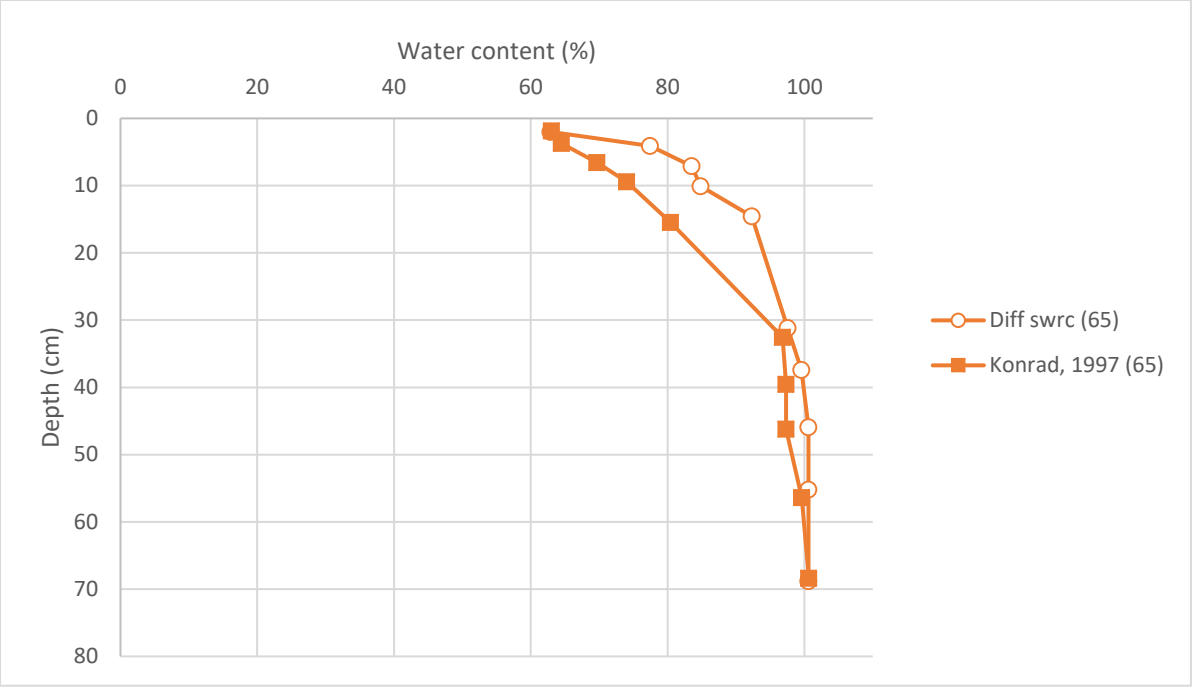

(d) 65 hours after evaporation

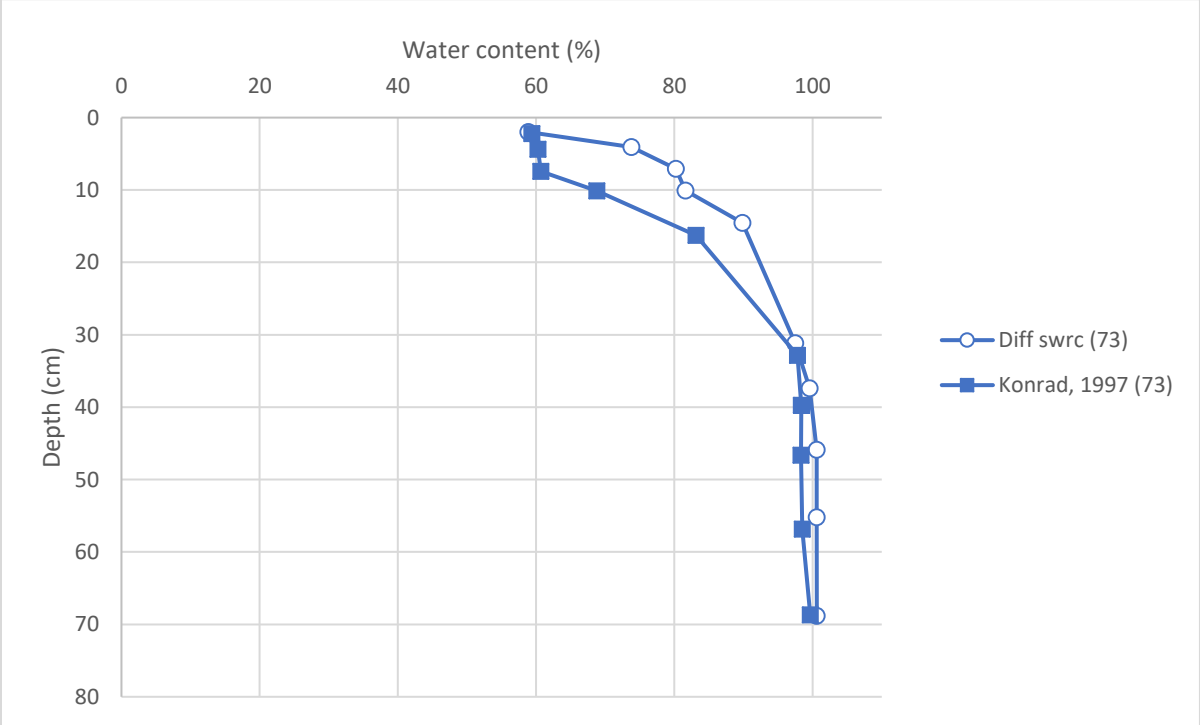

(e) 73 hours after evaporation

Figure 41 continued

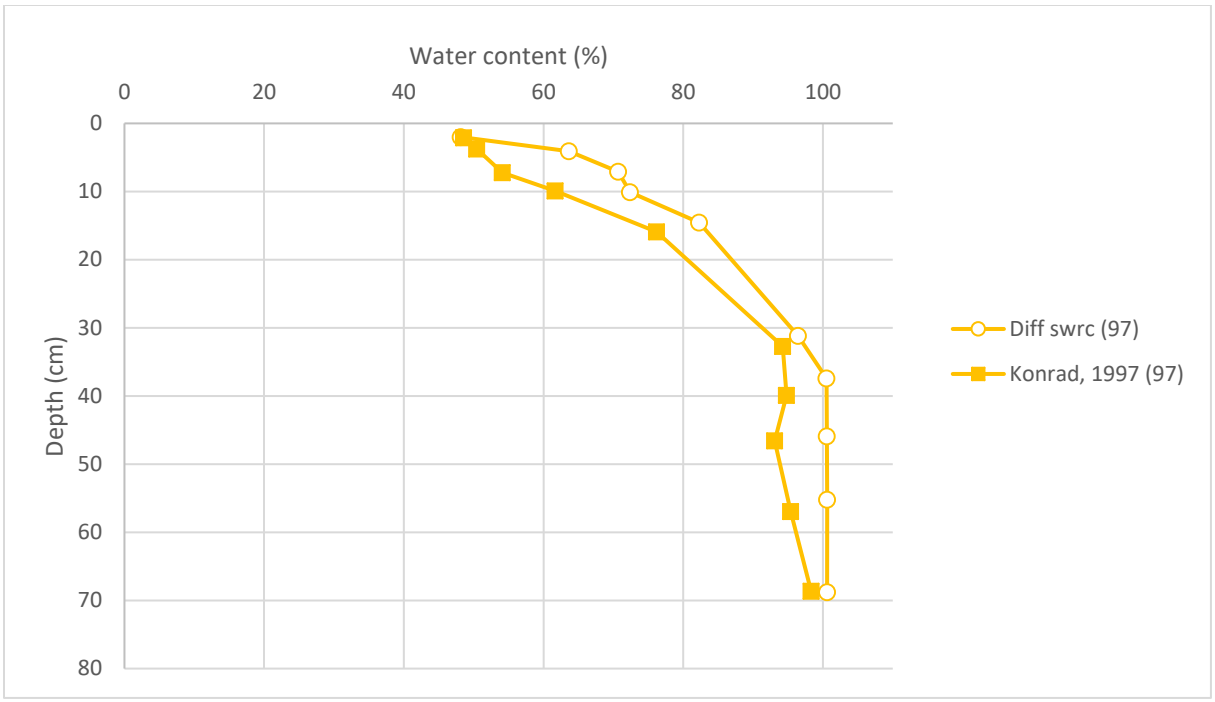

(f) 97 hours after evaporation

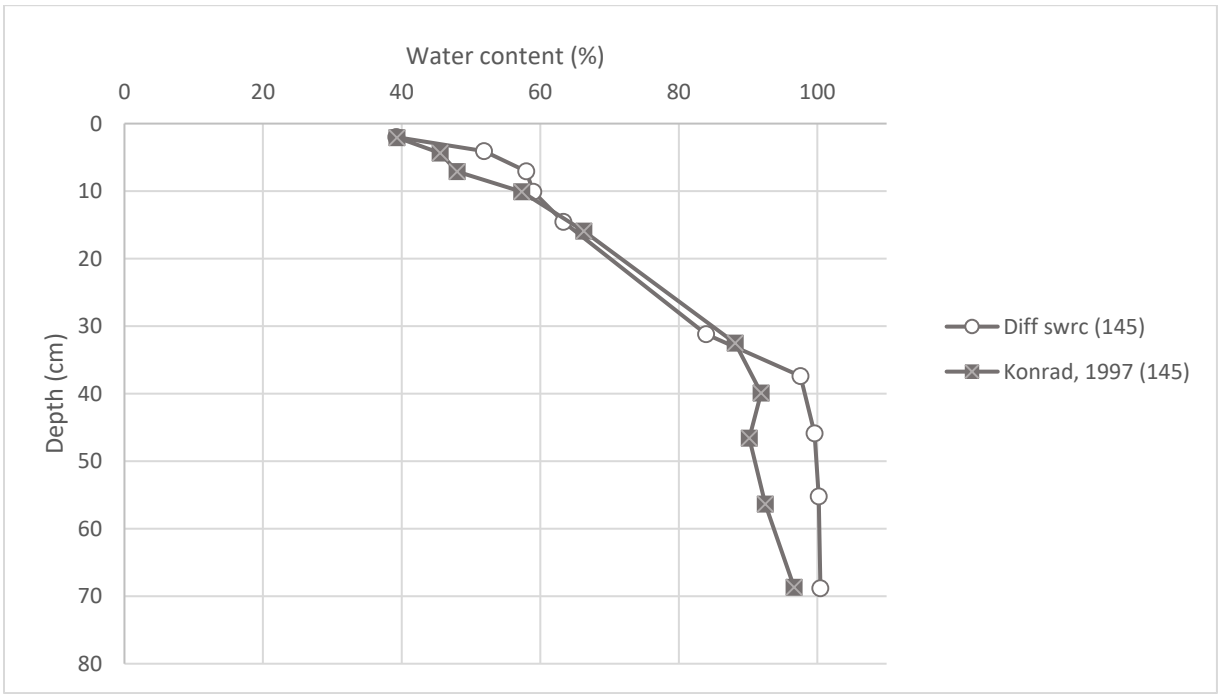

(g) 145 hours after evaporation

Figure 41 continued

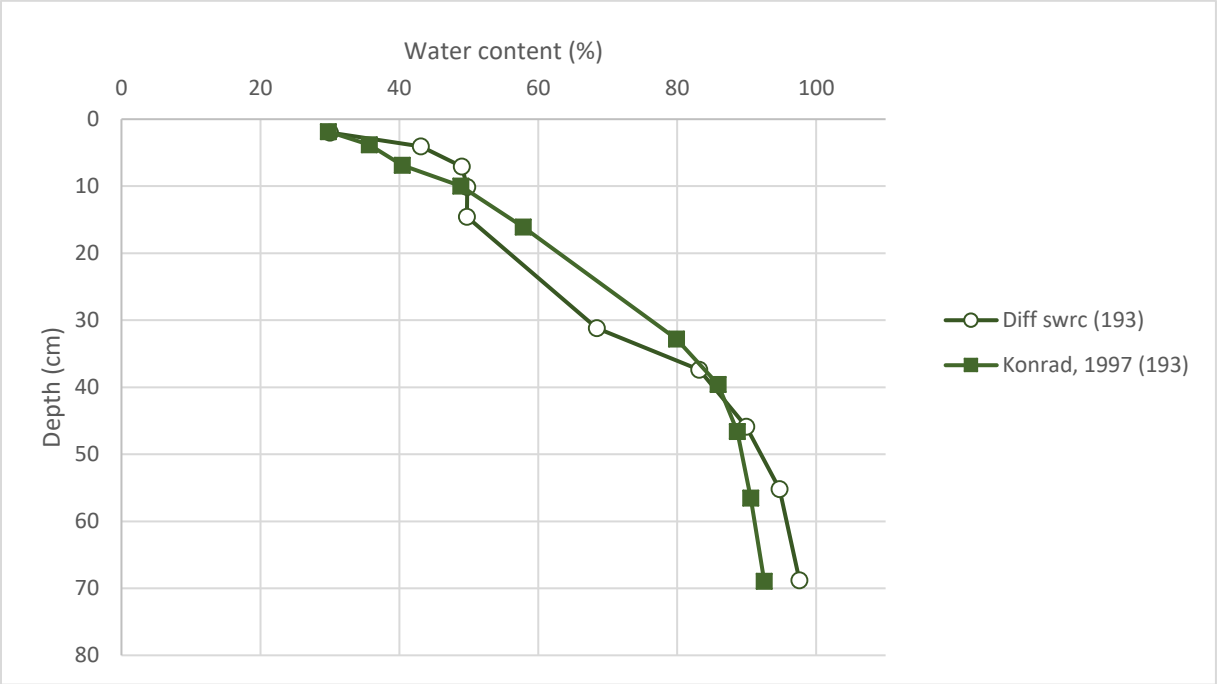

(h) 193 hours after evaporation

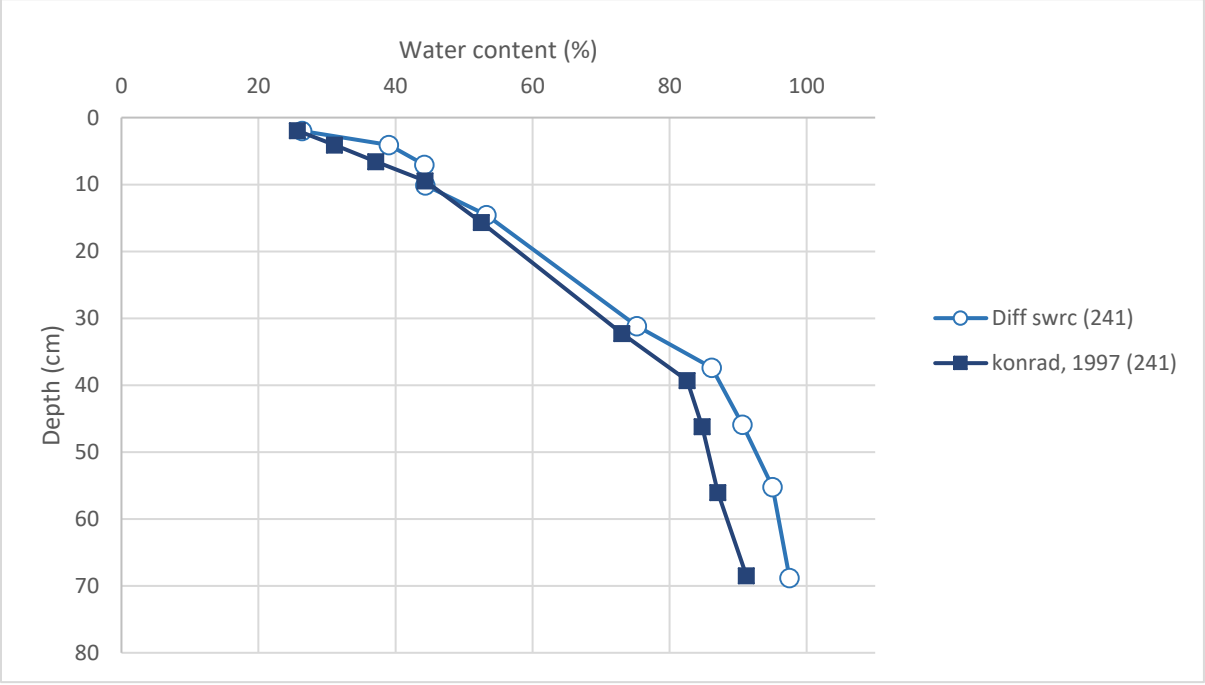

(i) 241 hours after evaporation

Figure 41 continued

The method to get water content profile in this research is as following,

1. Plotting line graph of degree of saturation between depth from 2 cm to 69 cm, which is same as the depth of TDR probes inserted in field test

2. Extracting data of degree of saturation of different elapsed time at depth where water content measured in field test in GID

3. Calculating water content of different elapsed time at same depth in step 2 with help of void ratio, specific gravity.

Even though the porosity have influence on formation of cracks(Stewart, Rupp, Abou Najm, & Selker, 2016), in this research, cracks are taken into consideration based on the data extraction prosses shown above. Thus, water content profile shown in Fig 41 is able to present hydraulic properties in field test.

6.4.2 Mechanical properties of excavation case

Based on BBM, settlement is checked in cracks section at depth of 2 cm. Fig 42 presents the matching results of settlement in excavation case. Circle point line is settlement data from field test while rhombus point line represents that from excavation model. Parameters used to input in this model is shown in Table 10 and 11. The trend of settlement data is similar even though there is difference between results of filed test and model. This difference maybe produced by temperature or three-dimensional effect. This model will input temperature and fracture model of shear in future to get a better settlement matching result.

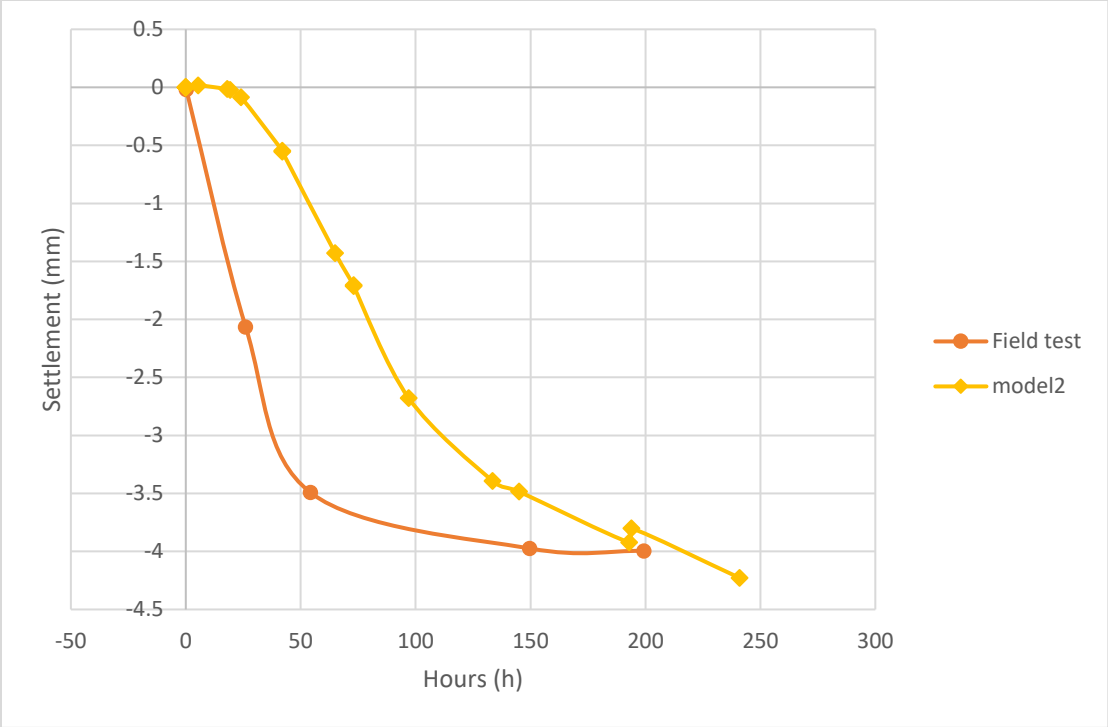

Figure 42. Settlement matching results at 2 cm depth with different elapsed time in excavation case

Table 10. Elastic parameters of BBM in excavation case

Elastic parameters of BBM					
κ_{i0}	κ_{s0}	α_i	α_{ss}	p_{ref}	υ
0.05	0.04	0	-1.5	0.10	0.42

Table 11. Mechanical parameters of interface element in excavation case

Mechanical parameters of interface element			
E (MPa)	υ	G_f (MN/m)	q_0 (MPa)
4	0	3.50E-7	0.01

6.4.3 Cracks formation and stress distribution in excavation case

After validating hydraulic and mechanical properties, cracks formation is observed in cracks section. Fig 43 illustrates cracks formation in cracks section. Space of cracks between cracks is varied from 9 cm to 29 cm while that in field test is 10 cm to 12 cm. Depth of propagated cracks is between 2 cm to 139 cm while that in field test is between 4 cm to 6 cm. It shows the model is able to approximately predict cracks propagation. And the scale of mesh is able to influence formation of cracks comparing the cracks formation in excavation case with that in simple case.

Figs. 44 and 45 presents the stress distribution before and after excavation, respectively. Stress distribution reorganize at top of the mesh, which makes it close to the field condition Fig 46 shows the stress distribution around cracks. It gives evidence that stress concentration at vicinity of cracks.

Figure 43. Cracks formation in cracks section

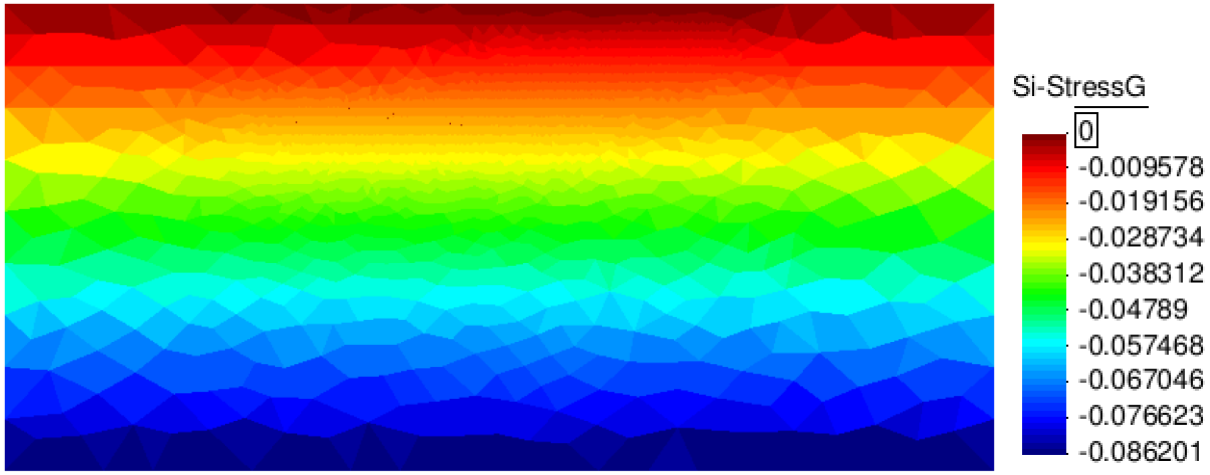

Figure 44. Stress distribution before excavation

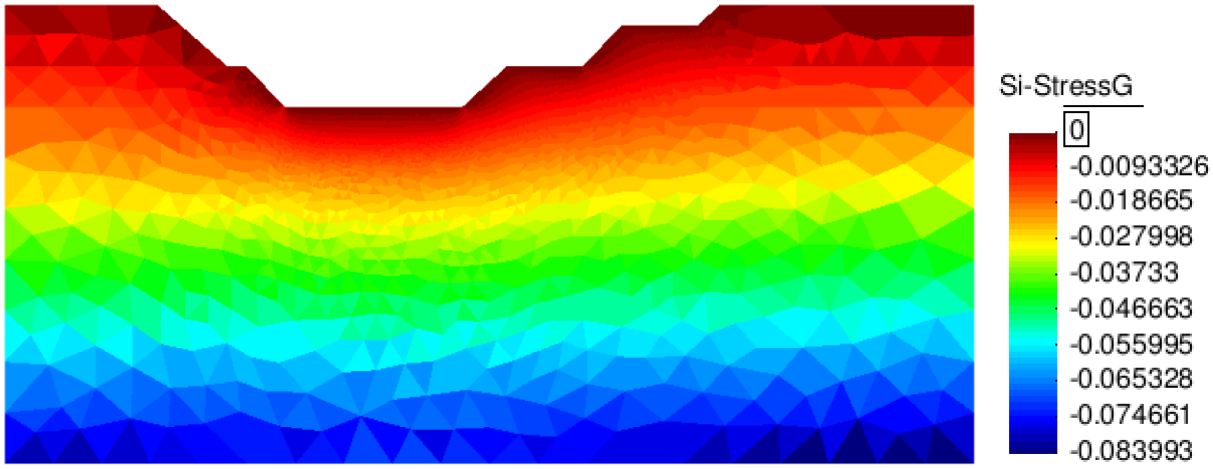

Figure 45. Stress distribution after excavation

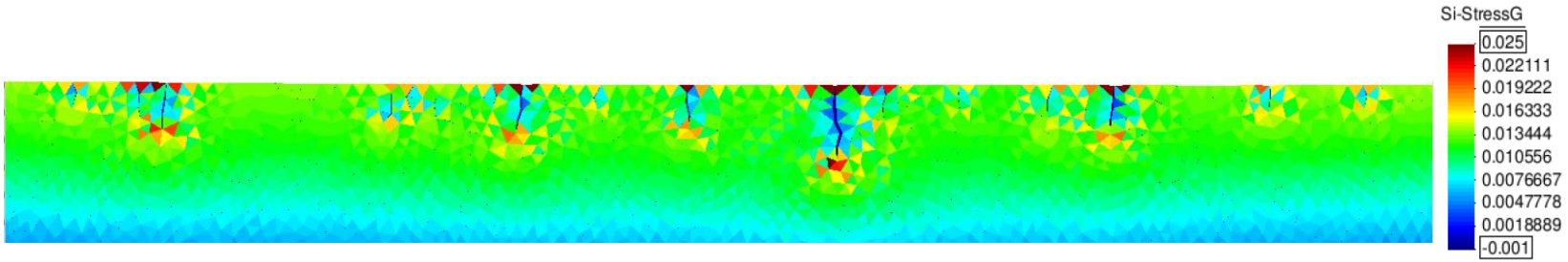

Figure 46. Stress distribution in cracks section

7. CONCLUSION AND FUTURE WORK

The Mesh Fragmentation Technique (MFT) was recently proposed by Sanchez et al. (2014) to simulate the formation and subsequent propagation of drying cracks in soils. It was shown that the MFT is capable of reproducing typical cracks morphologies typically observed in desiccated soils and the crack patterns obtained in small scale plate tests in the laboratory. Then this methodology was implemented by Maedo (2019) in the finite element code CODE_BIRGHT. In this research a fully coupled version of the MFT was used for first time to simulate and actual drying tests conducted under real environmental conditions and at large scale. The test selected corresponds to an excavation and drying experiment conducted in Canada and reported in Konrad (1997). The simple case and excavation case are used to validate the proposed framework. The simulation of this experiment has shown that the proposed framework is able to reproduce the reported variation of water content at different depths and also the settlements observed in this experiment. The model was also able to approximately predict the cracks depths and the spacing between cracks. However, the present study was not able to exactly reproduce the crack process in the field, and therefore, more research is needed to address this problem.

More parametric studies will finish in future to understand mechanism of BBM and HAR-FE. Temperature would be considered to get more accurate propagation of cracks. In addition, temperature may influence on this cracks propagation. After finishing the simulation on 2D stage, formation of cracks in 3D will be taken into consideration.

REFERENCES

Alonso, E. E., Gens, A., & Josa, A. (1990). A constitutive model for partially saturated soils G ". *Géotechnique*, *40*(3), 405–430. https://doi.org/10.1680/geot.1990.40.3.405

Cervera, M., Oliver, J., & Manzoli, O. (1996). A Rate-Dependent Isotropic Damage Model for the Seismic Analysis of Concrete Dams. *Earthquake Engineering & Structural Dynamics*, *25*(9), 987–1010. https://doi.org/10.1002/(SICI)1096-9845(199609)25:9<987::AID-EQE599>3.0.CO;2-X

Colina, H., De Arcangelis, L., & Roux, S. (1993). Model for surface cracking. *Physical Review B*, *48*(6), 3666–3676. https://doi.org/10.1103/PhysRevB.48.3666

Fredlund, D., Rahardjo, H., & Fredlund, M. (1993). Soil mechanics for unsaturated soils, 181–182.

Gens, A. (2000). Coupled Thermo-Hydro-Mechanical Analysis of Saline Materials . Application To Radioactive Waste. *Applied Sciences*, (September), 11–14.

Gens, A., Sánchez, M., Guimarães, L. D. N., Alonso, E. E., Lloret, A., Olivella, S., … Huertas, F. (2009). A full-scale in situ heating test for high-level nuclear waste disposal: observations, analysis and interpretation. *Géotechnique*, *59*(4), 377–399. https://doi.org/10.1680/geot.2009.59.4.377

Greve, A., Andersen, M. S., & Acworth, R. I. (2010). Investigations of soil cracking and preferential flow in a weighing lysimeter filled with cracking clay soil. *Journal of Hydrology*, *393*(1–2), 105–113. https://doi.org/10.1016/j.jhydrol.2010.03.007

Harris, G. L., Nicholls, P. H., Bailey, S. W., Howse, K. R., & Mason, D. J. (1994). Factors influencing the loss of pesticides in drainage from a cracking clay soil. *Journal of*

Hydrology, *159*(1–4), 235–253. https://doi.org/10.1016/0022-1694(94)90259-3

Hillerborg, A., Modéer, M., & Petersson, P. E. (1976). Analysis of crack formation and crack growth in concrete by means of fracture mechanics and finite elements. *Cement and Concrete Research*, *6*(6), 773–781. https://doi.org/10.1016/0008-8846(76)90007-7

Hueckel, B. T., & Borsetto, M. (1990). Thermoplasticity o f saturated soils and shales: constitutive equations. *Journal of Geotechnical Engineering*, *116*(12), 1765–1777. https://doi.org/10.1061/(ASCE)0733-9410(1990)116:12(1765)

Ingraffea, A. R., & Saouma, V. (1985). Numericak modelling of discrete crack propagation in reinforced concrete and plain concrete. *Fracture Mechanics of Cocnrete*, 171–225. https://doi.org/10.1007/978-94-009-6152-4_4

Jabakhanji, R., & Mohtar, R. H. (2015). A peridynamic model of flow in porous media. *Advances in Water Resources*, *78*, 22–35. https://doi.org/10.1016/j.advwatres.2015.01.014

Kindle, E. (1917). Some factors affecting the development of mud-cracks. *The Journal of Geology*, *25*(2), 135–144. Retrieved from http://www.jstor.org/stable/30060962 .%5Cnhttp://www.jstor.org/stable/10.2307/30060962

Kishné, A. S., Morgan, C. L. S., & Miller, W. L. (2009). Vertisol Crack Extent Associated with Gilgai and Soil Moisture in the Texas Gulf Coast Prairie. *Soil Science Society of America Journal*, *73*(4), 1221. https://doi.org/10.2136/sssaj2008.0081

Kitsunezaki, S. (1999). Fracture patterns induced by desiccation in a thin layer. *Physical Review E - Statistical Physics, Plasmas, Fluids, and Related Interdisciplinary Topics*, *60*(6), 6449–6464. https://doi.org/10.1103/PhysRevE.60.6449

Kodikara, J. K., & Choi, X. (2006). A simplified analytical model for desiccation cracking of clay layers in laboratory tests. In *Unsaturated soil 2006* (pp. 2186–2197). Retrieved from

https://ascelibrary.org/doi/abs/10.1061/40802%28189%29218

Konrad, J.-M., & Ayad, R. (1997). Desiccation of a sensitive clay: field experimental observations. *Canadian Geotechnical Journal*, *34*(6), 929–942. https://doi.org/10.1139/cgj-34-6-929

Konrad, J.-M., & Seto, J. T. C. (1993). Frost heave characteristics of undisturbed sensitive Champlain Sea clay. *Can.Geotech*, *31*, 285–298. https://doi.org/10.1139/t94-033

Kosmas, C., Moustakas, N., Kallianou, C., & Yassoglou, N. (1991). Cracking patterns, bypass flow and nitrate leaching in Greek irrigated soils. *Geoderma*, *49*(1–2), 139–152. https://doi.org/10.1016/0016-7061(91)90097-D

Lemaitre, J. (1984). A Three-dimensional ductile damage model applied to deep-drawing forming limits. *Mechanical Behaviour of Materials*, 1047–1053. https://doi.org/10.1016/B978-1-4832-8372-2.50132-9

Lemaitre, J. (1992). *A Course on Damage Mechanics*. https://doi.org/10.1007/978-3-662-02761-5

Lu, N., & Kaya, M. (2013). A drying cake method for measuring suction-stress characteristic curve, soil-water-retention curve, and hydraulic conductivity function. *Geotechnical Testing Journal*, *36*(1), 1–19. https://doi.org/10.1520/GTJ20120097

Lu, N., Şener-Kaya, B., Wayllace, A., & Godt, J. W. (2012). Analysis of rainfall-induced slope instability using a field of local factor of safety. *Water Resources Research*, *48*(9), 1–14. https://doi.org/10.1029/2012WR011830

Maedo, M. A., Manzoli, O. L., & Rodrigues, E. A. (2014). *Simulação computacional por elementos finitos de propagação de múltiplas fissuras em sólidos usando técnica de fragmentação da malha*. *Congresso Nacional de Engenharia Mecânica – CONEM*.

Manzoli, O. L., Maedo, M. A., Bitencourt, L. A. G., & Rodrigues, E. A. (2016). On the use of finite elements with a high aspect ratio for modeling cracks in quasi-brittle materials. *Engineering Fracture Mechanics*, *153*. https://doi.org/10.1016/j.engfracmech.2015.12.026

Manzoli, O. L., & Shing, P. B. (2006). A general technique to embed non-uniform discontinuities into standard solid finite elements. *Computers and Structures*, *84*(10–11), 742–757. https://doi.org/10.1016/j.compstruc.2005.10.009

Manzoli, O., Sánchez, M., Maedo, M., Hajjat, J., & Guimarães, L. J. N. (2018). An orthotropic interface damage model for simulating drying processes in soils. *Acta Geotechnica*, *13*(5), 1171–1186. https://doi.org/10.1007/s11440-017-0608-3

Miller, C. J., Mi, H., & Yesiller, N. (1998). Experimental analysis of desiccation crack propagation in clay liners. *Journal of the American Water Resources Association*, *34*(3), 677–686. https://doi.org/10.1111/j.1752-1688.1998.tb00964.x

Moës, N., & Belytschko, T. (2002). Extended finite element method for cohesive crack growth. *Engineering Fracture Mechanics*, *69*(7), 813–833. https://doi.org/10.1016/S0013-7944(01)00128-X

Moës, N., Dolbow, J., & Belytschko, T. (1999). A finite element method for crack growth without remeshing. *International Journal for Numerical Methods in Engineering*, *46*(1), 131–150. https://doi.org/10.1002/(SICI)1097-0207(19990910)46:1<131::AID-NME726>3.0.CO;2-J

Moran, M. S., T.R., C., Inoue, Y., & Vidal, A. (1994). Estimating crop water defficiency using the relation between surface minus air temperature and spectral vegetation index. *Remote Sens. Environ.*, *49*(49), 246–263. https://doi.org/10.1016/0034-4257(94)90020-5

Morris, P. H., Graham, J., & Williams, D. J. (1992). Cracking in drying soils. *Canadian*

Geotechnical Journal, *29*(2), 263–277. https://doi.org/10.1139/t92-030

Neely, H. L. (2014). Spatial and temporal distribution of desiccation cracks in shrink-swell soils, (May), 1–90.

Neely, H. L., Ackerson, J. P., Morgan, C. L. S., & McInnes, K. J. (2014). Instrumentation to Measure Soil Subsidence and Water Content in a Single Borehole. *Soil Science Society of America Journal*, *78*(4), 1251. https://doi.org/10.2136/sssaj2014.02.0055n

Neely, H. L., Morgan, C. L. S., Hallmark, C. T., McInnes, K. J., & Molling, C. C. (2016). Apparent electrical conductivity response to spatially variable vertisol properties. *Geoderma*, *263*, 168–175. https://doi.org/10.1016/j.geoderma.2015.08.040

Olivella, S., Carrera, J., Gens, A., & Alonso, E. E. (1994). Nonisothermal multiphase flow of brine and gas through saline media. *Transport in Porous Media*, *15*(3), 271–293. https://doi.org/10.1007/BF00613282

Olivella, S., Gens, A., Carrera, J., & Alonso, E. E. (1996). Numerical formulation for a simulator (CODE_BRIGHT) for the coupled analysis of saline media. *Engineering Computations (Swansea, Wales)*, *13*(7), 87–112. https://doi.org/10.1108/02644409610151575

Oliver, J. (1996). Modelling strong discontinuities in solid mechanics via strain softening constitutive equations. Part 1: Fundamentals. *International Journal for Numerical Methods in Engineering*, *39*(21), 3575–3600. https://doi.org/10.1002/(SICI)1097-0207(19961115)39:21<3575::AID-NME65>3.0.CO;2-E

Oliver, J., Huespe, A. E., & Cante, J. C. (2008). An implicit/explicit integration scheme to increase computability of non-linear material and contact/friction problems. *Computer Methods in Applied Mechanics and Engineering*, *197*(21–24), 1865–1889. https://doi.org/10.1016/j.cma.2007.11.027

Oller, S., Oñate, E., Oliver, J., & Lubliner, J. (1990). Finite element nonlinear analysis of concrete structures using a “plastic-damage model.” *Engineering Fracture Mechanics*, *35*(1–3), 219–231. https://doi.org/10.1016/0013-7944(90)90200-Z

Parks, M. L., Lehoucq, R. B., Plimpton, S. J., & Silling, S. A. (2008). Implementing peridynamics within a molecular dynamics code. *Computer Physics Communications*, *179*(11), 777–783. https://doi.org/10.1016/j.cpc.2008.06.011

Pereira, L. C., Guimarães, L. J. N., Horowitz, B., & Sánchez, M. (2014). Coupled hydro-mechanical fault reactivation analysis incorporating evidence theory for uncertainty quantification. *Computers and Geotechnics*, *56*, 202–215. https://doi.org/10.1016/j.compgeo.2013.12.007

Ringrose-voase, A. J., & Bullock, P. (1984). The automatic recognition and measurement of soil pore types by image analysis and computer programs. *Journal of Soil Science*, *35*(4), 673–684. https://doi.org/10.1111/j.1365-2389.1984.tb00624.x

Rots, J. G., Nauta, P., Kuster, G. M. A., & Blaauwendraad, J. (1985). Smeared Crack Approach and Fracture Localization in Concrete. *HERON, 30 (1), 1985*. Retrieved from https://www.narcis.nl/publication/RecordID/oai:tudelft.nl:uuid:746aba89-3566-4ade-9931-d6bbae0c05ea

Sánchez, M., Gens, A., & Guimarães, L. (2012). Thermal–hydraulic–mechanical (THM) behaviour of a large-scale in situ heating experiment during cooling and dismantling. *Canadian Geotechnical Journal*, *49*(10), 1169–1195. https://doi.org/10.1139/t2012-076

Sánchez, M., Manzoli, O. L., & Guimarães, L. J. N. (2014a). Modeling 3-D desiccation soil crack networks using a mesh fragmentation technique. *Computers and Geotechnics*, *62*, 27–39. https://doi.org/10.1016/j.compgeo.2014.06.009

Sánchez, M., Manzoli, O. L., & Guimarães, L. J. N. (2014b). Modeling 3-D desiccation soil crack networks using a mesh fragmentation technique. *Computers and Geotechnics*, *62*, 27–39. https://doi.org/10.1016/j.compgeo.2014.06.009

Simo, J. C., & Ju, J. W. (1987). Strain- and stress-based continuum damage models-II. Computational aspects. *International Journal of Solids and Structures*, *23*(7), 841–869. https://doi.org/10.1016/0020-7683(87)90084-9

Simo, J. C., Oliver, J., & Armero, F. (1993). An analysis of strong discontinuities induced by strain-softening in rate-independent inelastic solids. *Computational Mechanics*, *12*(5), 277–296. https://doi.org/10.1007/BF00372173

Stewart, R. D., Rupp, D. E., Abou Najm, M. R., & Selker, J. S. (2016). A Unified Model for Soil Shrinkage, Subsidence,and Cracking. *Vadose Zone Journal*, *15*(3), 0. https://doi.org/10.2136/vzj2015.11.0146

Towner, G. D. (1987). The mechanics of cracking of drying clay. *Journal of Agricultural Engineering Research*, *36*(2), 115–124. https://doi.org/10.1016/0021-8634(87)90118-1

van Genuchten, M. T. (1978). Calculating the unsaturated hydraulic conductivity with a new, closed-form analytical model. *Water Resour. Program, Dep. of Civ. Eng., Princeton Univ., Princeton, NJ*, (September), 35. Retrieved from https://www.nrc.gov/docs/ML0330/ML033070005.pdf

White, D. J., Musacchio, G., Helmstaedt, H. H., Harrap, R. M., Thurston, P. C., Van der Velden, A., & Hall, K. (2003). Images of a lower-crustal oceanic slab: Direct evidence for tectonic accretion in the Archean western Superior province. *Geology*, *31*(11), 997–1000. https://doi.org/10.1130/G20014.1